Remote Sensing of Environment 244 (2020) 111801

Contents lists available at ScienceDirect

Remote Sensing of Environment

journal homepage: www.elsevier.com/locate/rse

The Landsat Burned Area algorithm and products for the conterminous United States

Todd J. Hawbaker[a,*], Melanie K. Vanderhoof[a], Gail L. Schmidt[b], Yen-Ju Beal[a], Joshua J. Picotte[c], Joshua D. Takacs[a], Jeff T. Falgout[d], John L. Dwyer[e,1]

[a] U.S. Geological Survey, Geosciences and Environmental Change Science Center, Denver, CO 80225, United States of America
[b] KBR, Contractor to the U.S. Geological Survey, Earth Resources Observation and Science Center, Sioux Falls, SD 57198, United States of America
[c] ASRC Federal Data Solutions, Contractor to the U.S. Geological Survey, Earth Resources Observation and Science Center, Sioux Falls, SD 57198, United States of America
[d] U.S. Geological Survey, Core Science, Analytics, Synthesis, and Libraries; Denver, CO 80225, United States of America
[e] U.S. Geological Survey, Earth Resources Observation Science Center, Sioux Falls, SD 57198, United States of America

ARTICLE INFO

Edited by Marie Weiss

Keywords:
Landsat
Burned area
Fire
United States
Machine learning

ABSTRACT

Complete and accurate burned area map data are needed to document spatial and temporal patterns of fires, to quantify their drivers, and to assess the impacts on human and natural systems. In this study, we developed the Landsat Burned Area (BA) algorithm, an update from the Landsat Burned Area Essential Climate Variable (BAECV) algorithm. Here, we present the BA algorithm and products, changes relative to the BAECV algorithm and products, and updated validation metrics. We also present spatial and temporal patterns of burned area across the conterminous U.S., how burned area varies in relation to the number of operational Landsat sensors, and a comparison with other burned area datasets, including the BAECV, Monitoring Trends in Burn Severity (MTBS), GeoMAC, and Moderate Resolution Imaging Spectroradiometer (MODIS) MCD64A1.006 data. The BA algorithm identifies burned areas in analysis ready data (ARD) time-series of Landsat imagery from 1984 through 2018 using machine learning, thresholding, and image segmentation. Validation with reference data from high-resolution commercial satellite imagery resulted in omission and commission error rates averaging 19% and 41%, respectively. In comparison, validation with Landsat reference data had omission and commission error rates averaging 40% and 28%, respectively when burned areas in cultivated crops and pasture/hay land-cover types were excluded. Both validation tests documented lower commission error rates relative to the BAECV products. The amount of burned area detected varies not only in response to climate but also with the number of operational sensors and scenes collected. The combined amount of burned area detected by multiple sensors was larger than from any individual sensor, but there was no significant difference between individual sensors. Therefore, we used BA products from individual sensors to assess trends over time and all available sensors to compare with other existing BA products. From 1984 through 2018, annual burned area averaged 30,000 km^2, ranged between 14,000 km^2 in 1991 and 46,500 km^2 in 2012, and increased over time at a rate of 356 km^2/year. Compared to existing burned area products, the new Landsat BA products identified 29% more burned area than the BAECV products (1984–2015), 183% more than the MTBS/GeoMAC products (1984–2018), and 56% more than the MCD64A1.006 products (2003–2018). The products had similar patterns of year-to-year variability; the R^2 values of linear regressions between annual burned area were > 0.70 with the BAECV products and the MTBS/GeoMAC products, but somewhat lower for the MCD64A1.006 product (R^2 = 0.66). The BA products are routinely produced as new Landsat data are collected and provide a unique data source to monitor and assess the spatial and temporal patterns and the impacts of fire.

1. Introduction

Fires are discrete events with highly variable spatial and temporal occurrence patterns and wide-ranging impacts on human and social systems (Abatzoglou and Kolden, 2013; Abatzoglou and Williams, 2016; Dennison et al., 2014; French et al., 2014; Ghimire et al., 2012;

* Corresponding author.
E-mail address: tjhawbaker@usgs.gov (T.J. Hawbaker).
[1] Retired.

https://doi.org/10.1016/j.rse.2020.111801
Received 16 September 2019; Received in revised form 23 March 2020; Accepted 25 March 2020

Liu and Wimberly, 2015; Parthum et al., 2017; Picotte et al., 2016; Radeloff et al., 2018; Sankey et al., 2017; Shakesby and Doerr, 2006; Urbanski et al., 2018). Although many governmental agencies are tasked with reporting prescribed fires, and human-caused and natural wildland fires, there are few comprehensive data sources that consistently track fire occurrence over space and time (Brown et al., 2002; Fusco et al., 2019; Hawbaker et al., 2008; Short, 2015; Nowell et al., 2018). The incompleteness of fire data makes assessing trends and impacts of fires challenging. Thus, routine generation of data products that consistently track fires and the area they burn over time and across space are needed to understand their patterns, drivers, and consequences, as well as to project future potential changes (Chuvieco et al., 2019; Hollmann et al., 2013; Roy et al., 2014).

In 2017, the Landsat Burned Area Essential Climate Variable (BAECV) products were released. This was the first fire-related data product consistently generated on an annual time step for the conterminous U.S. (CONUS) using the entire pixel-level time series of all available Landsat 4, 5, and 7 images (Hawbaker et al., 2017). The BAECV algorithm was designed to identify burned areas ≥4 ha in both forest and non-forest ecosystems, differing from previous Landsat-based efforts to monitor disturbances that specifically target forest ecosystems (Hansen et al., 2014; Huang et al., 2010; Kennedy et al., 2010) and other change detection methods that map persistent land change (Zhu and Woodcock, 2014a) potentially missing burned areas that do not result in long-lasting spectral change (Zhu et al., 2019). The BAECV products demonstrated the capability of moderate-resolution satellites to generate fire information at scales relevant to managers and policy makers over durations needed to separate spurious changes from long-term trends. Furthermore, the BAECV products documented unique spatial patterns and rates of burning, indicating that burned area has increased by 130% over the past 3 decades but that the rate of increase may not have been as extreme as previously reported (Hawbaker et al., 2017). Compared to other fire monitoring efforts (Alonso-Canas and Chuvieco, 2015; Andela et al., 2018; Chuvieco et al., 2016, 2018, 2019; Eidenshink et al., 2007; Giglio et al., 2016, 2018; Long et al., 2019; Plummer et al., 2006; Roy et al., 2008; Schroeder et al., 2016; Short, 2013; Tansey et al., 2008), the BAECV products identified both large and small fires across CONUS with the spatial detail and temporal depth needed to understand which human and natural systems are being impacted by fires, to guide local and national fire policy, and to inform land management activities.

Validation of remote sensing products provides critical information to help users determine if data meets their needs and benchmark algorithm improvements (Morisette et al., 2006). The Committee on Earth Observing Satellites Working Group on Calibration and Validation (CEOS; https://lpvs.gsfc.nasa.gov/) defines validation as “the process of assessing, by independent means, the quality of the data products derived from the system outputs”. Recommendations for validation of global, coarse resolution burned area products (Boschetti et al., 2009) suggest collecting reference data from images that: (1) have higher spatial resolution and enough spectral resolution to identify burned areas, (2) span the time period of the products being validated, and (3) allows for use of paired images to separate recent burned areas from older burned areas and avoids confusion with other types of change. Validation of global, coarse resolution burned area products following these protocols typically use Landsat image pairs to develop reference data (Padilla et al., 2014, 2015; Boschetti et al., 2016; Padilla et al., 2017). Applying the CEOS validation protocols to Landsat products that span the entire length of the archive remains challenging if not impossible and alternative approaches are needed (Chuvieco et al., 2019). For validating Landsat products, aerial photography and commercial satellite imagery are the primary sources of high-resolution imagery to derive reference data from, but these data have not been collected systematically over the length of the Landsat archive and can be costly. Furthermore, it has not been demonstrated that it is feasible to use statistical sampling and image pairs with high-resolution imagery as was done in coarse resolution burned area product validations (Padilla et al., 2014; Boschetti et al., 2016; Padilla et al., 2017).

Because of the challenges of collecting high-resolution reference data, Landsat-derived reference data are commonly used to validate Landsat products (Stroppiana et al., 2012; Schroeder et al., 2016; Vanderhoof et al., 2017b; Long et al., 2019), although some have suggested that this approach is not strictly validation and is better described as product comparison or evaluation (e.g., Boschetti et al., 2015; Roy et al., 2019). Deriving reference data from Landsat imagery allows for validation of Landsat products over the entire length of the archive but is not without challenges. As with high-resolution imagery, visual interpretation of Landsat imagery can be difficult, especially when identifying small burned areas. This can be ameliorated by utilizing Landsat time series data and image pairs, consulting ancillary fire information, and having multiple experts develop the reference data (Cohen et al., 2010; Vanderhoof et al., 2017b; Pengra et al., 2019).

Collecting Landsat reference data following a statistical sampling design and using image pairs over the length of the archive and also collecting high-resolution post-fire reference data where available is the best possible compromise to meet the CEOS protocols. These are the approaches we took to validate the Landsat BAECV products. Vanderhoof et al. (2017a) validated the BAECV products with 286 high resolution images from 2003 through 2015 but were unable to use image pairs or validate products prior to 2003 because of limitations in how and when high resolution imagery has been collected across CONUS. Additionally, Vanderhoof et al. (2017b) used a reference dataset derived from Landsat image pairs at 28 path/rows and five years (1988, 1993, 1998, 2003, 2008) following the stratified sampling strategy suggested by Padilla et al. (2014, 2015).

The results of our previous BAECV validation studies found that detection rates varied with fire size: 50% or more of fires ≥10 ha were detected across CONUS and 70% of all fires ≥10 ha were detected across the western United States (Vanderhoof et al., 2017a). Errors of omission and commission for burned area averaged 42% and 33%, respectively, using the Landsat reference dataset (Vanderhoof et al., 2017a), and 22% and 48%, respectively, using the high-resolution reference dataset (Vanderhoof et al., 2017b). The BAECV omission and commission error rates were much lower than those found for global products which have documented omission and commission error rates ranging between 68% to 93% and 42% to 94%, respectively (Padilla et al., 2015). Coarse resolution burned area products have even higher error rates for the major biomes present across CONUS. For example, the Moderate Resolution Imaging Spectroradiometer (MODIS) burned area product (MCD45; Roy et al., 2008) performed well overall relative to other global burned area products; however, it performed poorly in temperate forest (99% omission, and 95% commission) and temperate grassland and savanna (87% omission, 69% commission), the land-cover classes dominating CONUS (Padilla et al., 2014). The lower commission and omission error rates of the BAECV products highlighted the potential to create both scene-level and annual composite burned area products from the Landsat archive that outperform coarse resolution burned area products. This finding was further confirmed by the Long et al. (2019) global map of burned areas generated with 2015 Landsat data in Google Earth Engine.

Since the release of the BAECV products, a few developments have necessitated changes to our approach. Here, we present the BA algorithm and products and highlight changes and improvements made from the BAECV algorithm and products. The first improvement involved bringing the BA products up to date because the existing products were only produced for 1984 through 2015. Users requested routine BAECV processing of new Landsat images as they were acquired. However, atmospherically corrected Landsat 8 Operational Land Imager (OLI) and Thermal Infrared Sensor (TIRS) data were not available during initial BAECV algorithm development. The algorithm could have been used as it is, however, with only ETM+ imagery. This was undesirable because of the scan-line-corrector (SLC) error gaps in

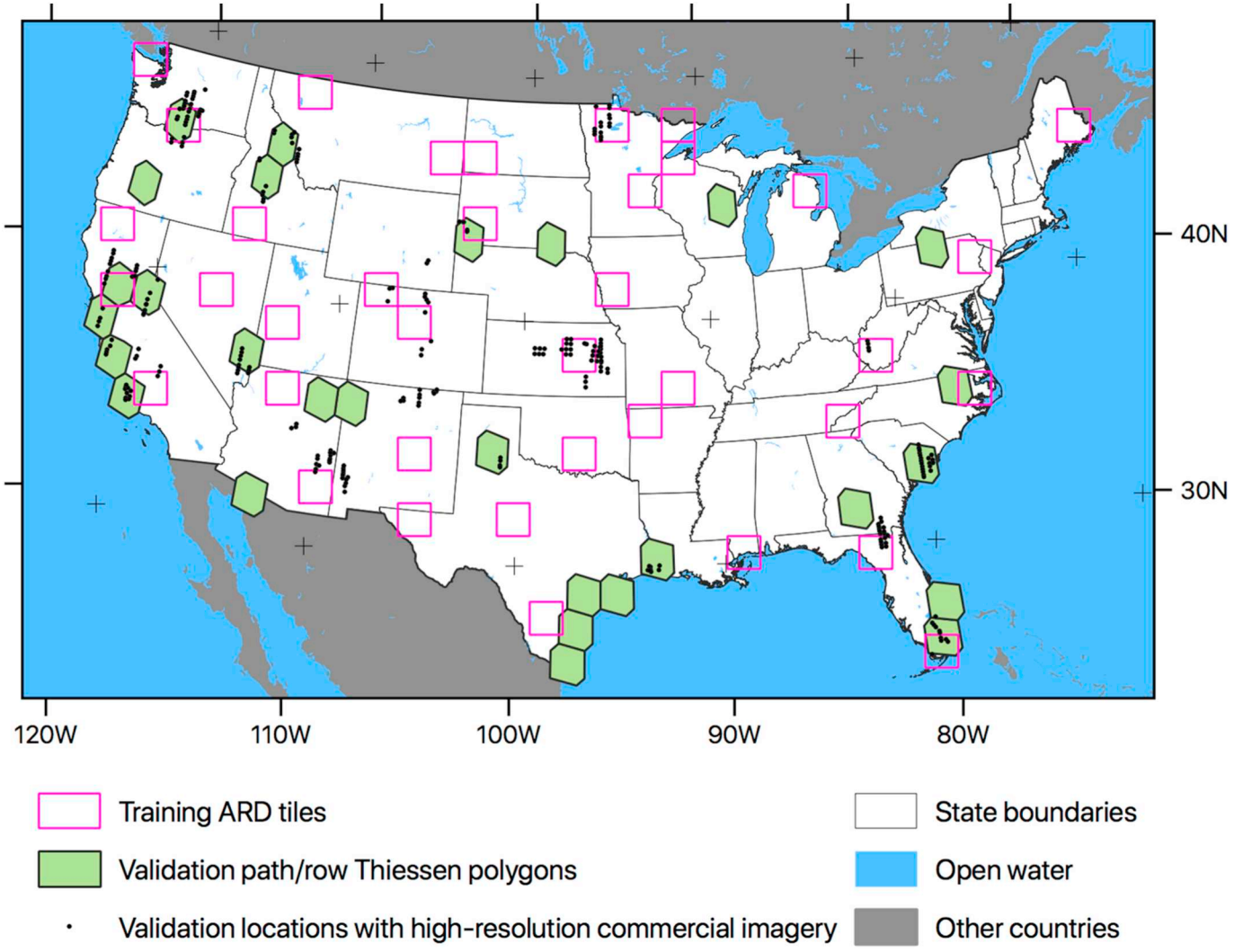

Fig. 1. Locations of Landsat Analysis Ready Data (ARD) tiles used for training the Landsat Burned Area algorithm, World Reference System path/row Thiessen polygons of areas where validation was performed using Landsat reference data, and areas where validation was performed using high-resolution commercial satellite imagery.

ETM+ imagery and exclusion of the more recent OLI/TIRS imagery. Surface reflectance data are now produced for OLI imagery using the Landsat 8 Surface Reflectance Code (LASRC; Vermote et al., 2016). Bringing the BA products up to date required algorithm adjustments to incorporate OLI/TIRS imagery, which also necessitated creation of new OLI/TIRS training and validation data to evaluate algorithm performance and update the validation metrics.

The second alteration we made to the algorithm was to incorporate the new Landsat analysis-ready data (ARD) delivery format (Dwyer et al., 2018) because the BAECV algorithm was designed to use the Landsat World Reference System (WRS-2) path/row format. Each ARD tile spans 5000 by 5000 pixels and crops all intersecting Landsat path/row images to the tile extent. The consistent size of ARD images eliminates the need to preprocess all images to a common spatial extent and facilitates the generation of temporal composites. Also, including all intersecting Landsat images in an ARD tile allows for more dense time-series data in areas with overlapping path/rows, potentially improving the effectiveness of variables based on summaries of historical conditions and change metrics. Furthermore, the ARD data are processed using consistent methods for geolocation, spatial alignment, radiometric calibration, atmospheric correction, and pixel quality assessment, eliminating the number of preprocessing steps performed by users of Landsat data (Dwyer et al., 2018).

In spite of the efficiencies provided by the ARD data and the availability of high-performance computing (Gorelick et al., 2017), processing the entire Landsat archive remains an arduous task and requires efficient approaches to apply algorithms to a large number of images; the archive held over ½ million individual Landsat 4, 5, 7, and 8 scenes covering CONUS for 1984–2018. The volume of data is amplified when using the ARD data because there are approximately 2000 images in an ARD time-series stack compared to approximately 500 images in a path/row time-series stack. One way to improve processing speed is to reduce the number of calculations made for each image in the time-series stack by limiting predictors used for burned area classification. For the BAECV algorithm, we selected spectral indices shown to be useful for mapping disturbances and burned areas based on previous studies. However, we did not consider all potential indices and many indices were correlated. The gradient boosting regression model (GBRM; Hastie et al., 2009) we used in the BAECV algorithm does not assume independence among predictors and can handle correlated variables; however, it is questionable whether inclusion of many variables and also highly correlated variables improved accuracy substantially. Therefore, in the BA algorithm, we introduced a suite of predictors especially tuned to ash and charcoal deposition after fire and changes in surface temperature. To limit the number of predictors used in the final model, we implemented a variable selection procedure to

reduce the number of predictors used, and thus also reduced computational demand.

Finally, we sought to improve accuracy to better meet the needs of users. In the BA algorithm, our efforts were focused on reducing commission error. As part of that effort, we also developed an additional filtering step to eliminate burned areas that were persistent over multiple years in the annual composites. Such areas would result in double counting and overestimating burned area. Once annual composites are filtered for persistent burned areas, we convert the rasters to vectors (fire perimeters) and attribute the perimeters with information to enable additional subsetting by users.

The Landsat BA algorithm follows the general approach outlined in Hawbaker et al. (2017), but with significant changes. As in the BAECV algorithm, a GBRM (Hastie et al., 2009) was used to estimate pixel-level burn probabilities, followed by a thresholding and segmentation process to classify each pixel as burned or not. In the BA algorithm, we altered the collection of training data, selection of predictor variables, and segmentation of the burn probability image. In this paper, we present details of changes made in the BA algorithm and validation methods, validation metrics, and products generated, as well as CONUS-wide spatial and temporal trends in burned area. The annual burned area detected in the Landsat BA products is also compared with other burned area products.

2. Methods

To train and evaluate the BA algorithm for the CONUS, we selected 38 ARD tiles that overlapped with the WRS-2 path/rows we used to train the BAECV algorithm (Fig. 1; Hawbaker et al., 2017). After training the BA algorithm, we used it to generate BA products from 1984 through 2018 for all ARD tiles covering the CONUS. Analyses were restricted to Tier 1 Level 1 Precision and Terrain (L1TP) corrected images with < 80% cloud cover. For validation of the BA products, we used the same approach used to validate BAECV products (Vanderhoof et al., 2017a,b). This included validation using a reference dataset derived from high-resolution (≤5-m resolution) satellite imagery for 286 images across CONUS (Vanderhoof et al., 2017a) and a second reference dataset derived from Landsat image pairs for 28 path/rows in CONUS (Vanderhoof et al., 2017b), updated to include 2013 OLI/TIRS image pairs. After validation, we assessed spatial and temporal patterns of burned area. To consider the potential influence of image count, the amount of burned area was also analyzed per sensor. Finally, we made comparisons among the BA products, the BAECV products, Monitoring Trends in Burn Severity (MTBS; Eidenshink et al., 2007) and GeoMAC data (www.geomac.gov), and the MODIS MCD64A1.006 (Giglio et al., 2018) data. Additional details of the various methods applied in this manuscript are provided in the following subsections and a flowchart of processing steps is provided in Fig. S1. The scene-level and annual composite burned area products are listed in Tables S1 and S2.

2.1. Predictor variables

In the BA algorithm, we included OLI scenes and used only the OLI bands that had spectral characteristics similar to the TM and ETM+ bands (see Table 1 for the band naming conventions used in this study). We also included a larger suite of spectral indices more specific to mapping burned areas (Table 2) but used the same general types of predictor variables as in the BAECV algorithm. These included (1) land surface conditions in each scene; (2) reference conditions that characterize the land surface prior to disturbances visible in each scene; and (3) change metrics quantifying the magnitude of change between the reference conditions and each scene. Scene-level predictors used by the BA algorithm included the spectral indices listed in Table 2. The reference variables represented pre-fire surface conditions using 3-year lagged means and standard deviations for each of the single-scene predictor variables. The change predictor variables included the difference between the values of a given predictor in a Landsat scene (e.g. normalized burn ratio, NBR) and its corresponding reference predictor (e.g. the 3-year lagged mean of NBR). Three-year lags were used as development of the BAECV products indicated that results were less noisy using 3-year lags than when using 1-year lags and would better represent pre-fire conditions early in the archive when temporal gaps between cloud-free observations can be large (Egorov et al., 2019). Surface reflectance products were used for spectral bands produced by the Landsat Ecosystem Disturbance Adaptive Processing System (LEDAPS; Masek et al., 2006) for TM and ETM+ and LASRC for OLI (Vermote et al., 2016). Top-of-atmosphere (TOA) thermal brightness temperature values were used because operational land surface temperature products were not yet available. Thermal brightness temperature values are delivered with 30-m resolution in the ARD data, resampled to match the resolution of the surface reflectance bands even though the resolution of the thermal band has varied between 60 m and 120 m across the Landsat sensors used in this study. Pixels flagged as cloudy, water, or snow/ice by the function of mask algorithm (FMask; Zhu and Woodcock, 2014b) were excluded from all calculations.

Table 1
Landsat Thematic Mapper (TM), Enhanced Thematic Mapper Plus (ETM+), and Operational Land Imager (OLI) and Thermal Infrared Sensor (TIRS) bands used by the Landsat Burned Area algorithm. NIR: near infrared, SWIR: shortwave infrared.

Band name	Wavelength (μm)		
	TM	ETM+	OLI/TIRS
Blue	0.45–0.52	0.45–0.52	0.45–0.51
Green	0.52–0.60	0.52–0.60	0.53–0.59
Red	0.63–0.69	0.63–0.69	0.64–0.67
NIR	0.76–0.90	0.77–0.90	0.85–0.88
SWIR1	1.55–1.75	1.55–1.75	1.57–1.65
Thermal	10.40–12.50	10.40–12.50	10.60–11.19
SWIR2	2.08–2.35	2.09–2.35	2.17–2.29

2.2. Training and evaluation data

The MTBS data (Eidenshink et al., 2007) were the primary source of known burned areas used to train the GBRM in the BA algorithm. The MTBS data only include large fires, defined as ≥2 km^2 in the eastern US and ≥4 km^2 in the western US. Data for each MTBS fire consist of a fire perimeter polygon and a categorical burn severity raster layer derived from either a single post-fire Landsat scene or a pair of pre- and post-fire Landsat scenes. The MTBS fires used for training the GBRM in this study spanned the Landsat 7 and 8 eras (1999–2015).

To generate the training data required by the GBRM, we selected point locations within each of the selected ARD tiles (Fig. 1). Points were spatially distributed between unburned and burned areas, as indicated by the MTBS polygon data. An initial set of point locations were randomly selected within burned areas at a rate of 1 point/100 burned pixels up to a maximum of 1500 points per ARD tile. The burned points were combined with the MTBS severity rasters (retaining points with low, moderate, or high burn severity) and perimeters (for fire dates). Unburned point locations were selected outside of the MTBS burned areas and also randomly stratified across the 1992 National Land Cover Database (NLCD; Vogelmann et al., 2001) classes. The unburned sampling rate was 1 point/1000 pixels in each NLCD class, up to a maximum of 100 points per NLCD class per ARD tile. There were on average 15 unique NLCD classes in each tile; so, this approach provided a nearly equal number of burned and unburned points in each ARD tile. All burned points were visually assessed with Landsat ETM+ and OLI scenes to confirm they were actually burnt areas. The burned and unburned points were combined; then predictor values were extracted for each point from the Landsat ETM+ and OLI scenes in the ARD time series. The amount of unburned data relative to burned data was

Table 2
Spectral indices tested as potential scene, reference, and change predictor variables in the Landsat Burned Area algorithm. See Table 1 for spectral and thermal bands used from the different Landsat sensors. NIR: near infrared, SWIR: shortwave infrared.

Name	Abbreviation	Formula	Reference
Burned Area Index	BAI	$1 / ((0.1 - Red)^2 + (0.06 - NIR)^2)$	(Chuvieco et al., 2002)
Char Soil Index	CSI	NIR / SWIR2	(Smith et al., 2007)
Enhanced Vegetation Index	EVI	$2.5 * (NIR - Red) / (NIR + (6.0 * Red) - (7.5 * Blue) + 1.0)$	(Huete et al., 2002)
Global Environmental Monitoring Index	GEMI	$\eta * (1.0–0.25 * \eta) - (Red - 0.125) / (1 - Red)$; $\eta = (2 * (NIR^2 - Red^2) + (1.5 * NIR) + (0.5 * Red)) / (NIR + Red + 0.5)$	(Pinty and Verstraete, 1992)
Mid InfraRed Burn Index	MIRBI	$(10.0 * SWIR2) - (9.8 * SWIR1) + 2.0$	(Trigg and Flasse, 2001)
Normalized Burn Ratio	NBR	$(NIR - SWIR2) / (NIR + SWIR2)$	(García and Caselles, 1991; Key and Benson, 2006)
Normalized Burn Ratio 2	NRB2	$(SWIR1 - SWIR2) / (SWIR1 + SWIR2)$	(García and Caselles, 1991; Key and Benson, 2006)
Normalized Burn Ratio Thermal	NBRT1	$(NIR - (SWIR2 * Thermal)) / (NIR + (SWIR2 * Thermal))$	(Holden et al., 2005)
Normalized Difference Moisture Index	NDMI	$(NIR - SWIR1) / (NIR + SWIR1)$	(Gao, 1996; Wilson and Sader, 2002)
Normalized Difference Vegetation Index	NDVI	$(NIR - Red) / (NIR + Red)$	(Tucker, 1979)
Normalized Difference Wetness Index	NDWI	$(Green - NIR) / (Green + NIR)$	(McFeeters, 1996)
Soil-Adjusted Vegetation Index	SAVI	$1.5 * (NIR - Red) / (NIR + Red + 0.5)$	(Huete, 1988)
Vegetation Index 6 Thermal	VI6T	$(NIR - Thermal) / (NIR + Thermal)$	(Holden et al., 2005)
NIR/red ratio	VI43	NIR / Red	(Tucker, 1979)
NIR/SWIR1 ratio	VI45	NIR / SWIR1	(Epting et al., 2005; Kushla and Ripple, 1998)
NIR/thermal ratio	VI46	NIR / Thermal	(Holden et al., 2005)
SWIR1/SWIR2 ratio	VI57	SWIR1 / SWIR2	(Epting et al., 2005; Kushla and Ripple, 1998)

excessive and fitting GBRMs to the entire time series was not practical. Therefore, we subset the points for each ARD by randomly selecting 12 unburned observations for each point and, if the point burned, only the first burned observation was retained. We also augmented the unburned sample with 100 random pixels marked as cloud, cloud shadow, water, and snow/ice by FMask per year to ensure these were well represented as unburned in our training data and that any cloud, cloud shadow, water, and snow/ice areas missed by FMask would not confuse the classification. Finally, we combined the points from the individual ARDs. This resulted in 127,776 points or an average of 3363 points per ARD tile. The combined points were split 50/50 into training and testing datasets prior to fitting the GBRM.

2.3. Scene-level burned area probability mapping

The BA algorithm used a GBRM to estimate the probability that each pixel in a Landsat ARD time series had burned. Training a GBRM requires specifying parameters for the (1) number of trees, (2) number of splits per tree, and (3) learning rate between successive trees (Hastie et al., 2009). In practice, setting these three parameters involves fitting models for a range of parameter values and then evaluating tradeoffs among model complexity, accuracy of predictions, and computation time. We selected a range of values for the learning rate (0.1, 0.05, and 0.01) and the number of splits per tree (1, 3, 5, and 7) parameters. For each combination of learning rate and number of splits per tree, we fit a GBRM with our training data using 2000 trees. After initial model fits, the number of trees used in each GBRM was systematically reduced by evaluating changes in the accuracy metric for the test data as a function of the number of trees, to determine the smallest number of trees needed to achieve the maximum value of the area under the curve (AUC) of receiver operator characteristic plots. We selected the GBRM parameter set that resulted in the highest accuracy with the lowest number of trees.

Even though GBRMs are capable of handling a large number of predictors, unimportant predictors, and highly correlated predictors, inclusion of additional predictors does come with the expense of the processing time required to calculate and make predictions with them. Additionally, inclusion of unimportant predictors is likely to introduce noise in the results (Murphy et al., 2010). Therefore, to train the GBRM for the BA algorithm, we implemented a stepwise forward variable selection routine to select the most important predictors (Elith et al., 2008; Ramo et al., 2018). Our routine sequentially tested a suite of potential predictors and selected the single predictor that increased the GBRM's AUC value most. During each step, remaining predictors to test were removed if they had a 0.95 or greater correlation with any of the selected predictors. This process continued until the change in AUC was < 0.001. Reference and change predictors for each spectral index were only considered after the scene-level spectral index was selected as a predictor. Once the final set of predictors was selected and used to train a GBRM, the GBRM was applied to all the Landsat scenes in each ARD to generate scene-level burn probability (BP) products (Table S1).

2.4. Scene-level burned area classification

Classification of burned areas within the burn probability images was performed using a combination of thresholding and image segmentation techniques, similar to the approach used with the BAECV algorithm (Hawbaker et al., 2017) and approaches taken by others (Chuvieco et al., 2002; Goodwin and Collett, 2014; Koutsias, 2003; Stroppiana et al., 2012). The first step in this process uses a conservative burn probability value (96%) to threshold the individual burn probability images into candidate burned areas. The candidate burned areas were then grouped into patches and patches < 2 ha (22 pixels) were removed; visual analyses indicated that this was a reasonable threshold. The remaining candidate burned area patches were allowed to spread into neighboring pixels with burn probability values $\geq 71\%$ using random walker segmentation (Grady, 2001). In the resulting scene-level burn classification (BC) products (Table S1), pixels with burn probability values $< 90\%$ were removed to ensure within-fire heterogeneity was maintained.

2.5. Validation of acquisition-level products

We validated the scene-level BA products (Table S1) using two independent reference datasets, following the same approaches used to validate BAECV products (Vanderhoof et al., 2017a,b). This included

using a reference dataset derived from 286 high-resolution images across CONUS (2003–2015; Vanderhoof et al., 2017a), and a second reference dataset derived from Landsat image pairs across 28 path/rows and six years (1988, 1993, 1998, 2003, 2008, 2013), updated with the 2013 image pairs from Vanderhoof et al. (2017b).

2.5.1. High-resolution reference data

High-resolution images with image acquisition dates between 2003 and 2015 were selected using a disproportionate sampling approach to increase the proportion of samples collected within rare cover classes, in this case burned areas. To find images containing burned areas, we targeted "hot spots" of burned areas or regions that frequently burn, as identified using the MTBS perimeters and MODIS active fire detections (MCD14ML.006; Giglio et al., 2016). Each DigitalGlobe (https://www.digitalglobe.com) and Planet (https://www.planet.com) image that contained a burned area was paired with a nearby image, that showed no burned area, to test for errors of commission. This second image was not necessarily collected on the same date as the nearby image. With this approach, we identified a total of 286 high-resolution images across the Arid West (45 images containing a burn, 45 with no burn), the Mountain West (33 images containing a burn, 33 with no burn), the Great Plains (34 images containing a burn, 34 with no burn), and the East (31 images containing a burn, 31 with no burn; Fig. 1). Because these images are not regularly collected, burned area extent was mapped from single images, not image pairs. The images were distributed between GeoEye-1 (n = 9, 2 m resolution), QuickBird-2 (n = 172, 2 m resolution), WorldView-2 (n = 73, 2 m resolution) and RapidEye satellites (n = 37, 5 m resolution). For images in which the dominant land-cover type, as defined by the 2011 NLCD, was grassland, agriculture or hay/pasture, the gap between the high-resolution image and corresponding Landsat image was limited to 5 days or less to reduce the possibility of confusing burned areas with other change in these cover types. The date gap between all high-resolution and Landsat images averaged 8 days.

The high-resolution imagery was processed in both PCI Geomatica and ENVI. Two programs were used due to changes in the availability of the atmospheric correction modules, mid-project. In PCI Geomatica, the imagery was atmospherically corrected and converted to ground reflectance using ATCOR (the Atmospheric Correction module; Richter and Schläpfer, 2016). In ENVI, imagery was atmospherically corrected and converted to ground reflectance using FLAASH (Adler-Golden et al., 1998, 1999). In both programs, burned area was identified using maximum likelihood supervised classification, in which each image was trained on manually selected "burned" and "unburned" polygons. A sieve filter, in PCI Geomatica, and a low-pass filter, in ENVI, were applied to reduce noise in the output images with the window size and pixel aggregation varying based on the amount of noise produced by each classification. Most images were filtered using a 5 × 5 window size. Classified images were then manually edited. Each classified high-resolution image was compared to the nearest, cloud-free (< 20% cloud cover) scene-level Landsat burn classification. Each Landsat burn classification was upsampled to 2 m resolution. Additional details on the development of the high-resolution reference dataset can be found in Vanderhoof et al. (2017a).

2.5.2. Landsat reference data

The Landsat reference dataset was developed across 28 Landsat path/rows and six years (1988, 1993, 1998, 2003, 2008, 2013) for a total of 168 Landsat image pairs (Fig. 1). Fires are rare events and the resulting burned area is difficult to capture in reference data when validation sites are selected with random sampling. Instead stratified sampling can improve efficiency when collecting reference data and reduce the variance of accuracy estimates (Padilla et al., 2014; Boschetti et al., 2016; Padilla et al., 2017). Therefore, we used a stratified, random, one-stage clustering sampling design where each cluster was defined by a Thiessen scene area (TSA; Stehman, 2009). The TSAs were stratified across the major Olson biomes (Olson et al., 2001) including (1) temperate forest, (2) Mediterranean forest, (3) temperate grassland and savannah, (4) tropical and subtropical grasslands and savannah, and (5) xeric/desert shrub. The TSAs selected within each biome were meant to represent high and low burned areas as specified by the Global Fire Emissions Database (GFED) version 3 (Giglio et al., 2009, 2010). Landsat image pairs were selected to detect changes incurred over the peak fire season and were limited to those with a root mean squared error (RMSE) < 10 m, < 20% cloud cover, and available as a L1T Surface Reflectance product. The fire season varied by ecoregion, peaking between June through August in the Arid West, July through September across the Mountain West, March through April and September through October in the Great Plains, and September through May across the East, with the post-image occurring in the peak fire season in 70%, 91%, 76%, and 98% of the image pairs, respectively (Vanderhoof et al., 2017b). The FMask from the Landsat surface reflectance product was applied to both images to mask out clouds, cloud shadows, snow and open water (Zhu and Woodcock, 2012, 2014b). "New" burned area (post-fire – pre-fire) maps were generated using the Burned Area Mapping Software (BAMS), which is a semi-automated algorithm developed by the University of Alcala, Madrid (Bastarrika et al., 2014). The Normalized Burn Ratio (NBR), Mid-infrared Burned Index (MIRBI), Global Environmental Monitoring Index (GEMI), and Normalized Difference Vegetation Index (NDVI) were utilized in a supervised classification. The algorithm was trained on manually selected polygons containing (1) clearly burned pixels and (2) spectrally similar but less distinct burned pixels. The algorithm applied a region-growing function between the two types of training polygons, while cut-off values for each variable were extracted from the training polygons. Because no independent reference data were available for burned areas in agricultural cover types, the Landsat-based BAMS reference dataset did not train on agricultural fires and consequently cannot be considered accurate for this cover type. Following classification, the "new" burned areas were visually assessed and manually edited. Each image pair was classified into a burned area map and edited independently by three different analysts. When calculating validation metrics, a pixel was classified as burned if it was identified as burned by two of the three analysts. The "new" burned area reference data were compared to the "new" BA product burned area calculated by subtracting the corresponding scene-level burned area images. The inclusion of a Landsat-based reference dataset was essential to systematically validate the product across space and over the entire time series. Additional details on the development of the Landsat reference dataset can be found in Vanderhoof et al. (2017b). Using the validation hierarchy established by the Committee on Earth Observation Satellites Land Product Validation subgroup, this validation represents a Stage 4 validation where the reference datasets validate the product over a significant set of locations and time periods to quantify and characterize the uncertainties in the product (Morisette et al., 2006). Furthermore, the validation results have been updated to characterize the updated Landsat Burned Area product.

2.5.3. Validation metrics

Validation metrics included errors of omission and commission and relative bias for the burned category. To account for the influence of stratification and clustering (Stehman, 1997), the pixel-level accuracy metrics were calculated for each TSA or image, individually. Standard errors were then estimated to account for the stratified sampling design (Stehman et al., 2007). The general estimator for each accuracy metric was defined as the stratified combined ratio estimator (Cochran, 1977):

$$\widehat{R} = \frac{\sum_{h=1}^{H} K_h \overline{y_h}}{\sum_{h=1}^{H} K_h \overline{x_h}} \quad (1)$$

where H is the number of strata, K_h is the size of stratum h, $\overline{y_h}$ and $\overline{x_h}$ are the sample means of y_t and x_t of stratum h, and y_t and x_t are the

numerator and denominator of each accuracy metric equation, respectively (Padilla et al., 2014). The estimated variance of $\hat{R}$ was in turn defined as:

$$\hat{V}(\hat{R}) = \frac{1}{\hat{X}^2} \sum_{h=1}^{H} \frac{K_h^2}{k_h(k_h - 1)} \sum_{t \in h} d_t^2 \quad (2)$$

where k_h is the number of images sampled in stratum h and $\hat{X}$ and d_t are defined as:

$$\hat{X} = \sum_{h=1}^{H} K_h \overline{x_h} \quad (3)$$

$$d_t = (y_t - \overline{y_h}) - \hat{R}(x_t - \overline{x_h}) \quad (4)$$

Lastly, the standard error was calculated as:

$$SE = \sqrt{\hat{V}(\hat{R})} \quad (5)$$

We calculated validation metrics using both of the reference datasets. Comparisons were made between the previous BAECV and the new BA validation metrics with the high-resolution reference data for CONUS and four regions of the CONUS (Arid West, East, Great Plains, and Mountain West). Comparisons were made between the previously published BAECV validation metrics (Vanderhoof et al., 2017b) and the newly calculated BA validation metrics across CONUS and by land-cover class using Landsat reference data from 1988 through 2008 (2013 reference data were not assessed in the original BAECV validation study). Finally, we present validation metrics for the BA products for CONUS using the 1988 through 2013 Landsat reference data.

2.6. Annual composites

Burn probability and classification products were generated for each Landsat scene in the ARD time series from 1984 through 2018. The large number of scenes in these time series can make them unwieldly for visualization and analysis. Consequently, we also generated several products that are annual composites of the scene-level products (Table S2). These include (1) the per-pixel maximum burn probability (BP), (2) the burn classification count (BC) or the per-pixel count of the number of scenes that were classified as burned in a year, and (3) the burn date (BD) or the day of year (1–366) of the collection date of the first scene in which a pixel was classified as burned. The annual composites were generated from the scene-level products for each sensor individually (TM, ETM+, and OLI/TIRS) and also combining the scene-level products from TM and ETM+ and ETM+ and OLI/TIRS. The sensor-specific annual composites were not entirely independent as our algorithm uses multiple historical variables that were derived from all available sensors.

In the BAECV products, burned areas sometimes persisted from previous years, especially late-season fires. In the BA algorithm, we added a filter to remove the residual burned areas. This step identifies contiguous clusters of burned pixels in the annual BC images and produces a new output: filtered burn classification (BF). Burned area clusters that had > 33% overlap with clusters in the previous year were removed and added to the previous year's BF image. This step was implemented for ecoregions where burned areas are persistently visible over multiple years in Landsat images. These include the following Omernik Level I ecoregions (Omernik and Griffith, 2014): Northern Forests (5), Northwestern Forested Mountains (6), Marine West Coast Forests (7), Eastern Temperate Forests (8), Mediterranean California (11), Southern Semi-Arid Highlands (12), and Temperate Sierras (13).

The annual composites initially showed some large and obvious commission errors. Some appeared to be caused by artifacts not masked in the Landsat quality assurance bands, but in other areas, were likely caused by misclassification from our algorithm (Fig. 2). To remove these excessive commission errors, we visually examined results for each Landsat scene and flagged them for removal when they contained large commission errors. This step ranked scenes from high to low by the percentage of clear pixels that were classified as burned. Scenes with > 1.0% burned (n = 11,625) were visually assessed, starting with the highest percentage burned and working down. Each scene was flagged as acceptable or not based on visual analysis of the original Landsat scene and the corresponding burn probability and burn classification products. When necessary, we also consulted other fire data sources such as the MODIS active fire detections (MCD14ML.006; Giglio et al., 2016) and MTBS perimeters (Eidenshink et al., 2007) and GeoMAC perimeters (www.geomac.gov). After all scenes were assessed, annual composites were regenerated excluding any scenes flagged as unacceptable.

2.7. Vector products

In addition to the scene and annual raster products (Tables S1 and S2), we also created a version of the annual BF layer vectorized using an eight-neighbor rule to generate burned area polygons. Each burned area polygon was attributed with a count of 30-m pixels in the BF patch, and the minimum, maximum, mean, and standard deviation of the BC, BD, and BP annual composite values within the BF patch. Additional attributes in the vectorized BF product include the majority value from the Level III ecoregion layer (Omernik and Griffith, 2014) and the count of pixels in each NLCD class (Vogelmann et al., 2001; Yang et al., 2018). The version of NLCD used depended on the year of the annual BA product (Table S3). Because NLCD classifications varied over time, we also aggregated the counts by the original NLCD values to reclassified values common across NLCD versions (Table S4).

2.8. Assessing patterns of burning and differences among datasets

We assessed the overall spatial patterns of burned areas across CONUS from 1984 through 2018. Annual trends in burned area may be influenced by the number of operational Landsat sensors. Therefore, prior to assessing annual trends in burned area, we first determined the annual count of unique path/row scenes used by the BA algorithm across CONUS for each sensor. Then, we quantified the amount annual burned area that was mapped in the annual composites of the scene level products for each individual sensor and all sensors combined. We compared the annual scene count and area burned between time periods where (A) 1984–1998 when TM4 and TM5 were operational, to (B) 2000–2011 when TM5 and ETM+ were operational, and (C) 2014–2018 when ETM+ and OLI/TIRS were operational. Within time periods where 2 sensors were operational, we used 2-sided *t*-tests to determine if burned area was significantly different between individual sensors and from the combined results.

We also compared patterns among the BA data, the BAECV data, the MTBS data, and the MODIS MCD64A1.006 data (Giglio et al., 2018). Differences in data availability limited the years over which we made comparisons. Specifically, comparisons between the BA and BAECV data were limited to 1984–2015, the temporal range of the BAECV data. Because MTBS data were only available from 1984 to 2016, we augmented them with rasterized GeoMAC perimeters from 2017 and 2018 (www.geomac.gov) and made comparisons with the BA data for 1984–2018. The MTBS and GeoMAC data are collected differently. MTBS perimeters and burn severity rasters are manually delineated using Landsat data (Eidenshink et al., 2007). The GeoMAC data are initially generated by incident management teams using a wide range of mapping methods, then collected, standardized, and acquired by the U.S. Geological Survey (USGS). The GeoMAC data include both large and small fires and can contain multiple perimeters for individual fires (collected on different dates). We selected the final GeoMAC perimeter based on the last date and retained only large fires to be consistent with the MTBS methodology (≥ 4 km^2 in the West and ≥ 2 km^2 in the East). We limited comparisons with the MODIS MCD64A1.006 data to 2001–2018.

Finally, we assessed differences in the date of burned area detection

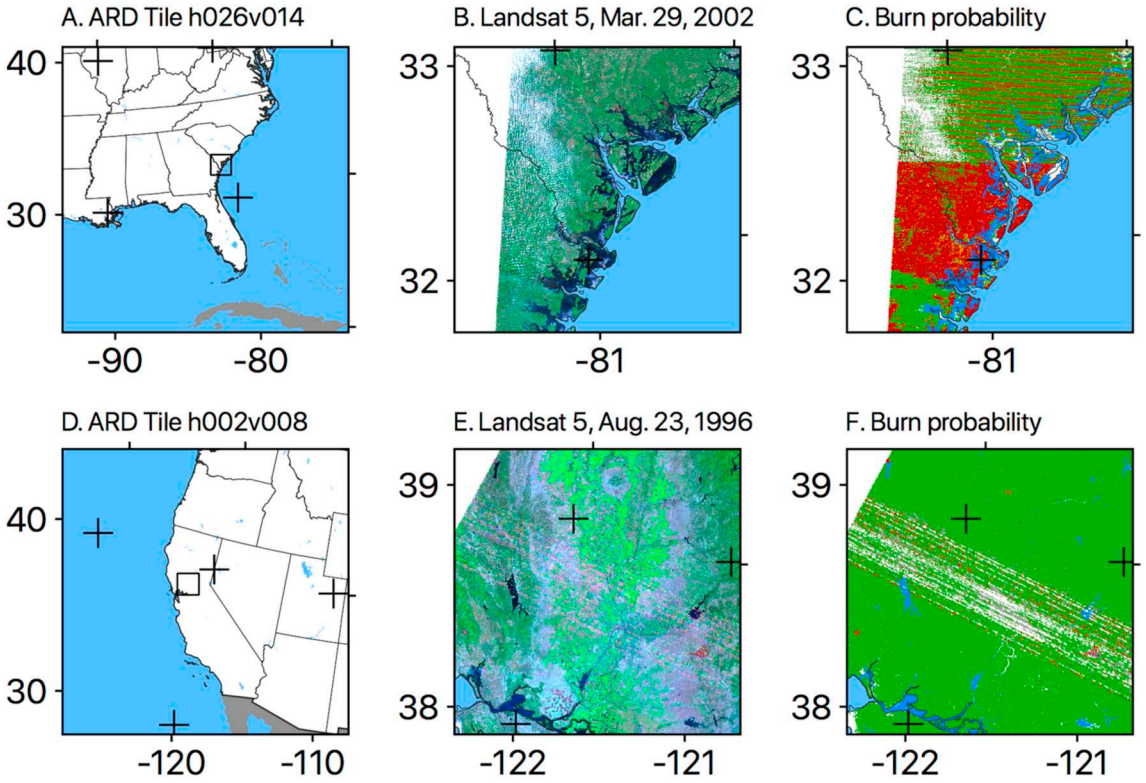

Fig. 2. Example of commission errors caused by poor image quality and sensor artifacts for Analysis Ready Data (ARD) tile h026v014 (A), Landsat 5 data from March 29, 2002 (B), and high burn probability values (C). Also, for ARD tile h002v008 (D), Landsat 5 data from August 23, 1996, and high burn probability values (F). Red areas in subfigure C and F indicate high burn probability. (For interpretation of the references to colour in this figure legend, the reader is referred to the web version of this article.)

between the BA annual composite burn date products and dates reported in both the Fire Program Analysis (FPA) Fire Occurrence Database (FOD) from 1992 to 2015 (Short, 2015) and the MCD14ML.006 active fire detections from 2001 to 2018. We used the FPA-FOD data instead of the MTBS data because they include point locations with dates for both large and small fires whereas the MTBS data only include large fires. However, we excluded FPA-FOD fires < 2 ha, the minimum burned area patch size in the Landsat BA products.

3. Results

3.1. Algorithm performance

Tests of model parameters indicated that the GBRM fit was maximized when using 1000 trees with three splits/tree and a 0.1 learning rate. These parameters were then used in a GBRM to select predictor variables. The final suite of predictors included eight variables (Fig. 3 for selected predictors and Table 2 for predictor descriptions). The predictor variables selected included NBRT1 and its 3-year lagged mean and standard deviation, VI45 and its 3-year lagged mean, NDVI and its 3-year lagged mean, and VI6T. The scene-level NBRT1 and VI45 predictors had the highest relative importance of the eight predictors. All of the predictors were based on the red, near infrared, shortwave infrared, and thermal bands. More than half the predictors included the thermal band (VI6T, NBRT1, and the 3-year lagged mean and standard deviation of NBRT1). Model fit measured with AUC was high (0.91) when the first predictor was selected (NBRT1), increased substantially to 0.97 as the second predictor was added (3-year lagged mean of NBRT1), and slowly leveled off as additional predictors were added to 0.99.

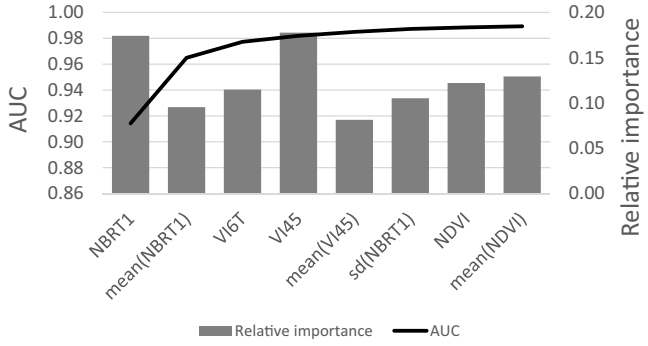

Fig. 3. The solid black line shows changes in area under the curve (AUC) of receiver operator characteristic plot as variables were added using stepwise forward selection. Grey bars show the relative importance of predictor variables in the final model. NBRT1: normalized burn ratio thermal; VI6T: near infrared/thermal ratio, VI45: near infrared/short-wave infrared ratio; NDVI: normalized vegetation index. Mean and sd indicate 3-year lagged mean and standard deviation of the specified spectral index.

3.2. Validation results with high-resolution imagery

Validation of the BA products using the 2003–2015 high-resolution reference data showed an overall increase in performance across CONUS compared to the BAECV products (Table 3). Based on these reference data, the BA products had 19% omission error (3% decrease from the BAECV products) and 41% commission error (7% decrease). The 3% decrease in omission error is within the standard error estimates of the two products. Across CONUS, the relative bias decreased by 27% compared to the BAECV products; however, because the commission error of the BA products exceeded omission error in most regions relative bias remained positive (39%).

Table 3
Validation statistics for the Landsat Burned Area Essential Climate Variable (BAECV) and Burned Area (BA) products, based on comparison with reference data derived from high-resolution commercial satellite imagery for 2003–2015 for the conterminous US (CONUS) and regions of CONUS. Standard errors are provided in parentheses (n = 286).

Region	Version	Omission error (%)	Commission error (%)	Relative bias (%)
CONUS	BAECV	22 (4)	48 (3)	66 (10)
CONUS	BA	19 (3)	41 (3)	39 (7)
Arid West	BAECV	14 (4)	36 (6)	34 (19)
Arid West	BA	16 (1)	44 (3)	50 (12)
East	BAECV	46 (3)	48 (5)	3 (13)
East	BA	45 (3)	37 (5)	−12 (11)
Great Plains	BAECV	13 (13)	70 (5)	194 (27)
Great Plains	BA	7 (13)	41 (3)	57 (19)
Mountain West	BAECV	22 (3)	39 (5)	27 (13)
Mountain West	BA	23 (3)	34 (5)	17 (5)

When analyzed regionally, error metrics for almost all regions showed improvement in the BA products (Table 3). Visually portraying patterns and errors for national-scale products is challenging; therefore, the examples shown in the figures were selected to (1) best represent regional error rates and differences in error rates between products, and (2) provide visual examples of the BA products in different regions. Omission errors changed little in most regions; the Great Plains was the only region with substantial changes with 6% lower omission error in the BA products than in the BAECV products, but standard errors were also relatively large. Changes in commission error were more prevalent. In the Great Plains, commission error was 29% lower and relative bias decreased substantially here from 194% to 57%. In the East, commission error decreased by 11%, but relative bias changed from 3% to −12%. A visual example of this type of change is shown in Fig. 4 where commission error was lower in the BA products than in the BAECV products for the Sweat Farm Road and Big Turnaround Complex fires, which burned in 2007 in Florida. In the Mountain West, commission error decreased by 5% and relative bias decreased by 10%. The Arid West was the only region that experienced an increase in commission error between the BA and BAECV products (8%); however, the differences between products in this region can be difficult to visually discern as they identify similar fire patterns (Fig. 5).

3.3. Validation with Landsat imagery

To ensure we were making appropriate comparisons between the BA and BAECV products, we initially limited validation analyses to Landsat reference data from 1988 to 2008 used in Vanderhoof et al. (2017b). Validation of the BA products using the 1988–2008 BAMS reference data in CONUS showed minimal change in omission error

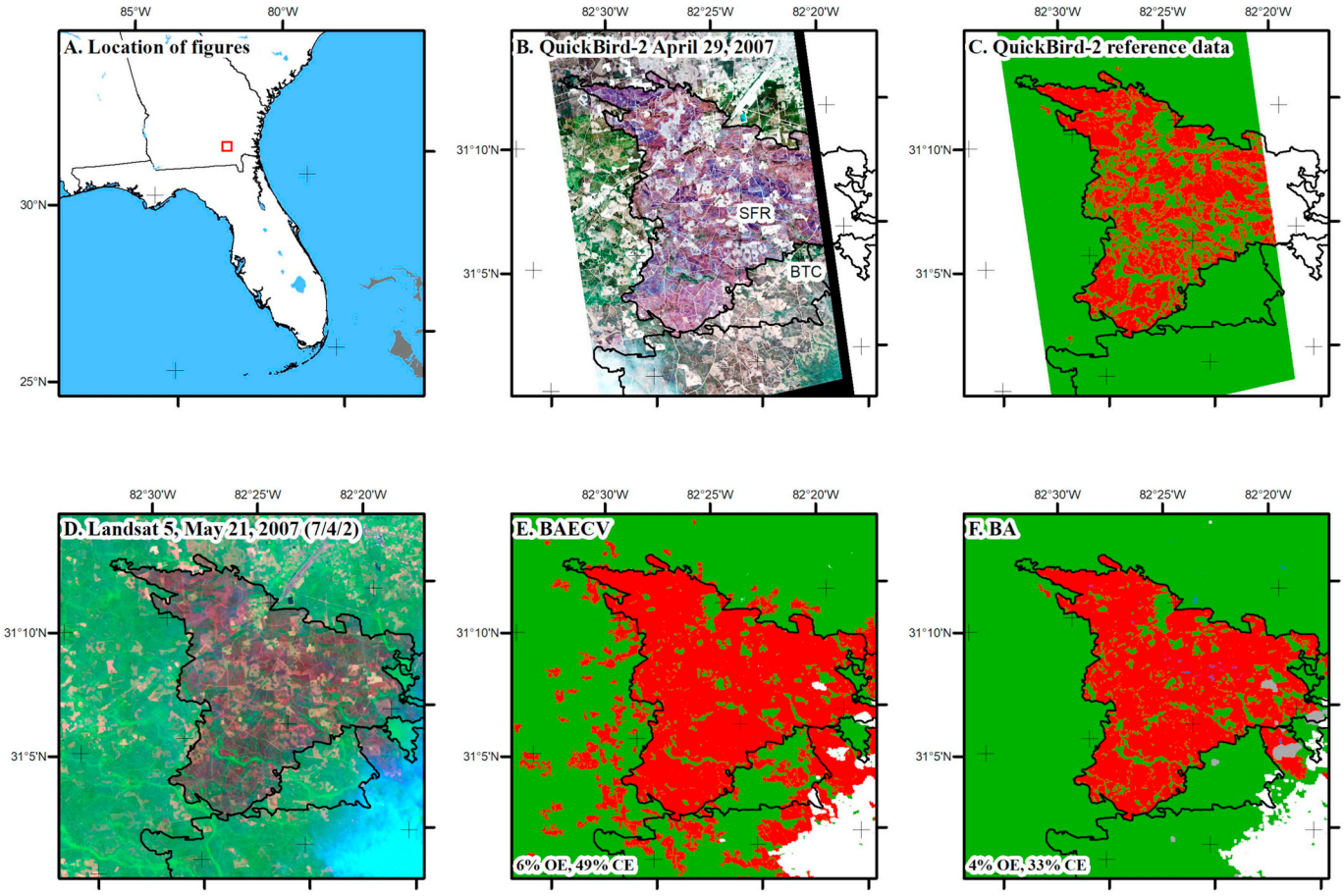

Fig. 4. Example of high-resolution validation data and comparison with Landsat Burned Area Essential Climate Variable (BAECV) and Burned Area (BA) products, including (A) location of figures; (B) QuickBird-2 imagery collected on April 29, 2007; (C) reference burned area data derived from QuickBird-2 imagery with burned areas shown in red; (D) Landsat 5 Thematic Mapper imagery collected on May 21, 2007; (E) Landsat Burned Area Essential Climate Variable (BAECV) classification; and (F) Landsat Burned Area (BA) classification. Monitoring Trends in Burn Severity perimeters are outlined in black for the Sweat Farm Road (SFR) fire (started April 16, 2007) and the Big Turnaround Complex (BTC) fire that burned in Okefenokee National Wildlife Refuge (started May 5, 2007). Omission error (OE) and commission error (CE) are shown in subfigure E and F for the BAECV and BA products, respectively. (For interpretation of the references to colour in this figure legend, the reader is referred to the web version of this article.)

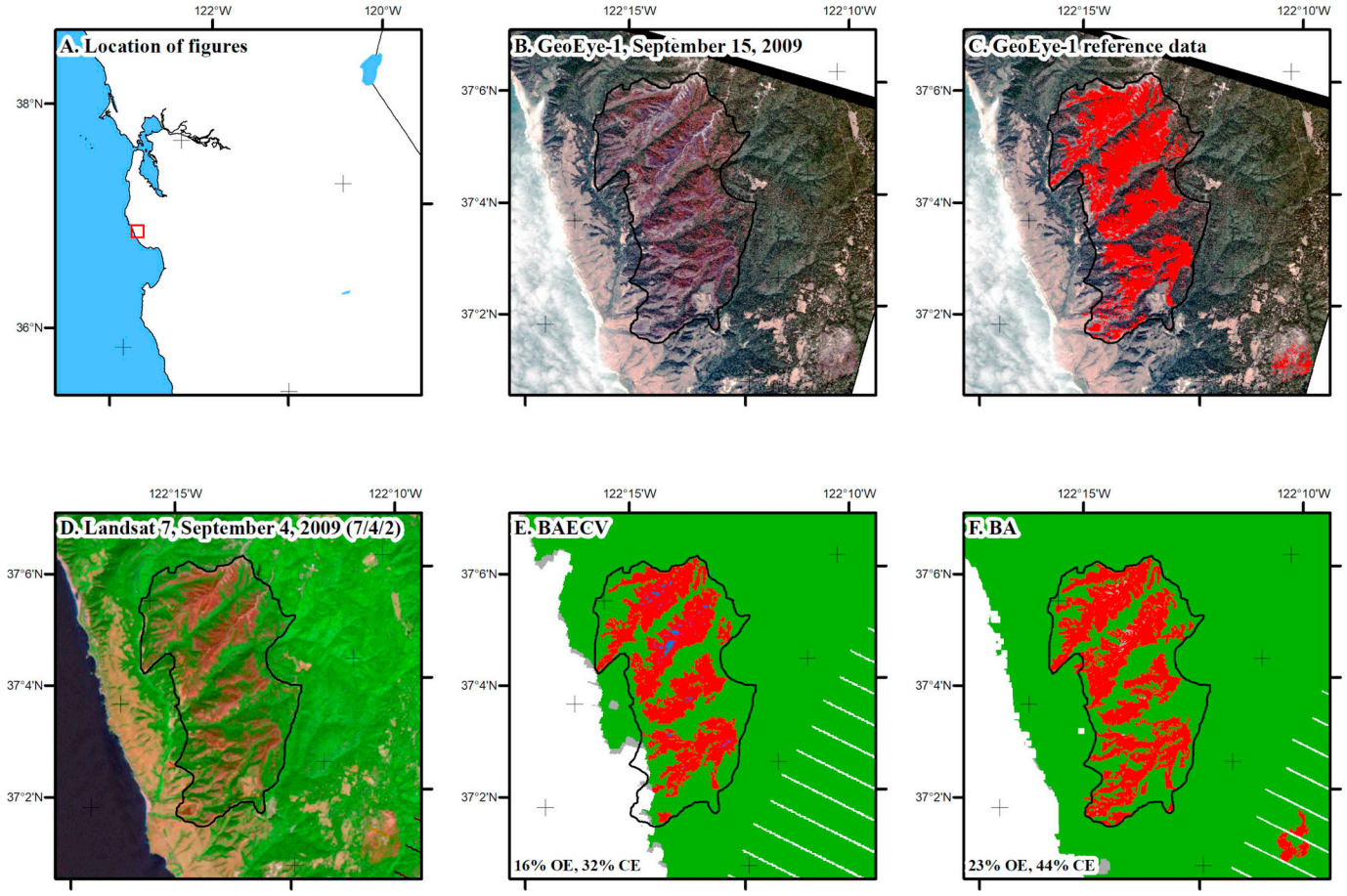

Fig. 5. Example of high-resolution validation data and comparison with Landsat Burned Area Essential Climate Variable (BAECV) and Burned Area (BA) products, including (A) location of figures; (B) GeoEye-1 imagery collected on September 15, 2009; (C) reference burned area data derived from GeoEye-1 imagery with burned areas shown in red; (D) Landsat 7 Enhanced Thematic Mapper Plus imagery collected on September 4, 2009; (E) Landsat Burned Area Essential Climate Variable (BAECV) classification; and (F) Landsat Burned Area (BA) classification. The Monitoring Trends in Burn Severity perimeter for the Lockhead fire (started Aug. 12, 2009) is outlined in black. Omission error (OE) and commission error (CE) are shown in subfigure E and F for the BAECV and BA products, respectively. (For interpretation of the references to colour in this figure legend, the reader is referred to the web version of this article.)

Table 4
Validation statistics for the Landsat Burned Area Essential Climate Variable (BAECV) and Burned Area (BA) products, based on comparison with reference data derived from Landsat imagery from 1988 to 2008 for the conterminous US (CONUS) and regions of CONUS. Standard errors are provided in parentheses. Values show the mean of each accuracy statistic across all of the Theissen scene area polygons in CONUS used for validation (n = 28).

Exclusions	Version	Omission error (%)	Commission error (%)	Relative bias (%)
None	BAECV	42 (6)	33 (3)	−14 (8)
None	BA	44 (6)	44 (7)	0 (16)
Cultivated crops, pasture/hay	BAECV	39 (6)	29 (3)	−15 (8)
Cultivated crops, pasture/hay	BA	40 (6)	27 (7)	−18 (17)
Cultivated crops, pasture/hay, prior years fires	BA	41 (6)	25 (7)	−20 (17)

(44% in the BA products vs. 42% in the BAECV products) and an increase in commission error (44% vs. 33%; Table 4). Because omission and commission errors were equal in the BA products, relative bias was zero. However, the increases in omission and commission error were troubling. Based on Vanderhoof et al. (2017b), mapping burned areas with Landsat in agriculture and pasture cover classes is challenging, even with visual analysis. This makes the BAMS reference dataset inaccurate in these cover classes. Additionally, validation statistics by land-cover type (Table 5) showed that commission errors increased by 10% in the pasture/hay cover class and relative bias was very high in both the pasture/hay and cultivated crops cover classes (121% and 126%, respectively). This increase is apparent when the BAECV and BA products are compared (Figs. 6 and 7). Therefore, we calculated the validation statistics with those two cover classes excluded (Table 4). Errors of omission and commission for the BA products, with pasture/hay and cultivated crops excluded, were similar, within 2% of the BAECV validation statistics.

In developing the algorithm, we added a step to remove burned areas detected in prior years, potentially reducing commission error. Comparisons between validation statistics show that excluding burned areas from prior years lowered commission error by an additional 2% in the BA products from 27% to 25%, but with the expected consequence of increased omission error by 1% (Table 4). After excluding pasture/hay and cultivated crops cover classes and removing burned areas from prior years, relative bias was −20% suggesting that the BA products provide a conservative estimate of burned area across CONUS.

The BA products incorporated OLI imagery from 2013 forward; consequently, we also generated validation statistics for CONUS and

Table 5
Validation statistics by land-cover class for the Landsat Burned Area Essential Climate Variable (BAECV) and Burned Area (BA) products based on comparison with reference data derived from Landsat imagery from 1988 to 2008 for the conterminous US (CONUS) and regions of CONUS.

Land-cover class	Version	Area burned (%)	Omission error (%)	Commission error (%)	Relative bias (%)
Cultivated crops	BAECV	6	90	88	−15
Cultivated crops	BA	26	73	88	121
Pasture/hay	BAECV	3	51	70	63
Pasture/hay	BA	3	54	80	126
Grasslands/ herbaceous	BAECV	21	40	32	−11
Grasslands/ herbaceous	BA	14	44	26	−24
Shrub/scrub	BAECV	32	32	23	−12
Shrub/scrub	BA	26	30	21	−12
Deciduous forest	BAECV	3	33	34	2
Deciduous forest	BA	2	29	35	8
Mixed forest	BAECV	6	20	20	0
Mixed forest	BA	6	17	24	10
Evergreen forest	BAECV	24	40	33	−11
Evergreen forest	BA	19	41	34	−11
Emergent wetlands	BAECV	4	76	33	−63
Emergent wetlands	BA	3	78	31	−68
Woody wetlands	BAECV	2	39	31	−12
Woody wetlands	BA	2	51	31	−30

regions within CONUS based on the updated Landsat reference data from 1998 to 2013, excluding burned areas in pasture/hay and cultivated crops cover classes, and excluding burned areas from prior years (Table 6). These statistics show that omission error was greater than commission error across CONUS (40% vs. 28%), resulting in a relative bias of −17%. The validation statistics varied regionally. Across all regions, relative bias was negative because omission errors were greater than commission errors. Relative bias was lowest in the Arid West (−4%) because omission errors (30%) roughly balanced commission errors (27%). The Mountain West had the next lowest relative bias (−22%) as a result of higher omission error (41%) but similar commission errors compared to the Arid West. In the East, omission error (61%) was greater than commission error (41%) resulting in a relative bias of −34%. Relative bias was largest in the Great Plains (−49%), where commission error was 33% and omission error was the highest across all regions (66%). Example comparisons of raw Landsat OLI imagery, BAMS reference data, and BA products are shown in Fig. 8. These examples show that the BAMs reference data and the Landsat BA products usually map the same burned patches, but with pixel-level differences in burned area around margins of patches.

3.4. Assessing spatial and temporal patterns of burning

The filtered product was used to assess the spatial and temporal patterns in the BA products. In this step, a total of 12,063 scenes with ≥0.010 proportion burned were examined; 4167 of those scenes were excluded because of excessive commission errors, which represents <

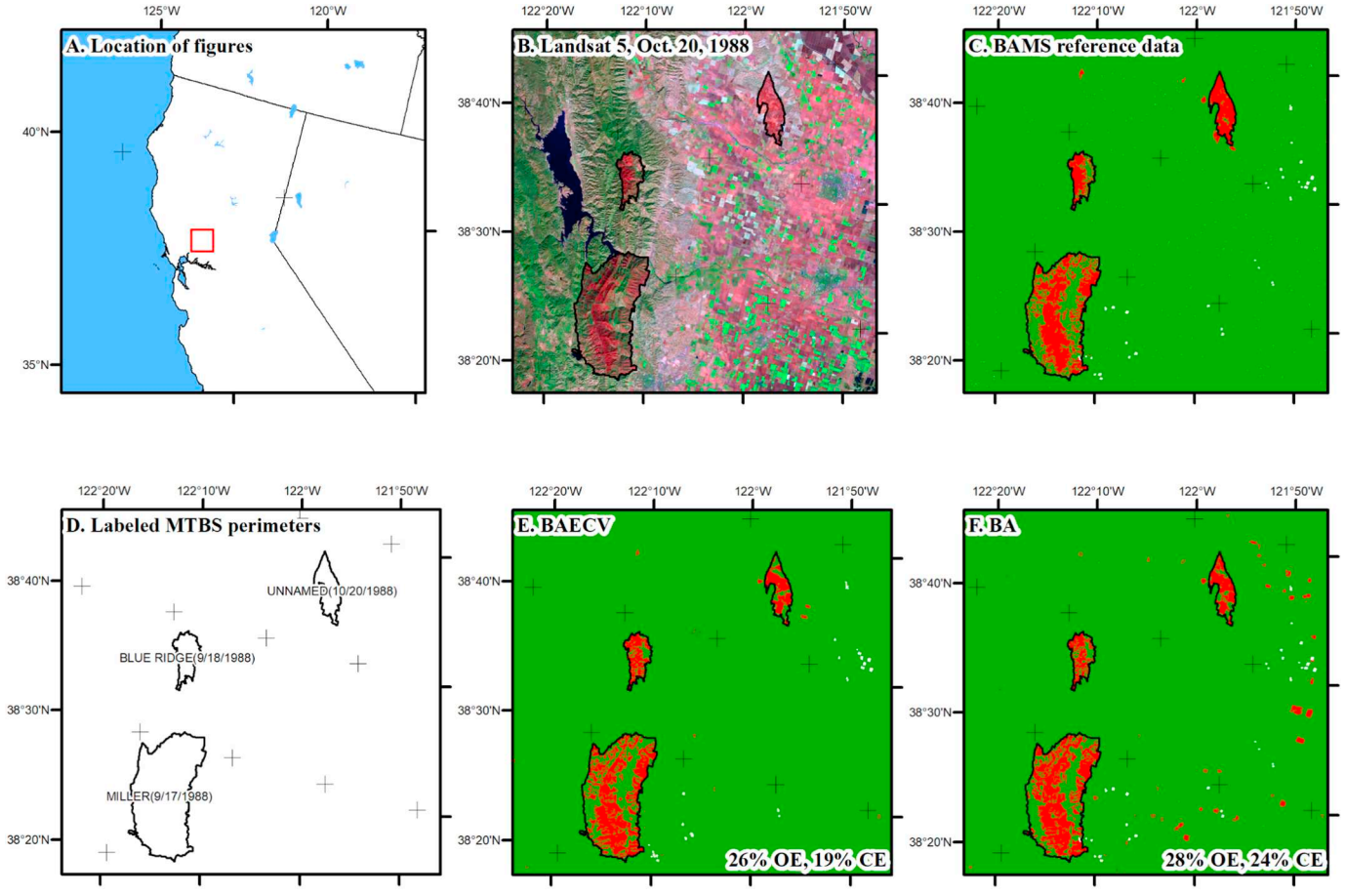

Fig. 6. Example of Landsat-based BAMS reference data with Landsat burned area products, including (A) location of figures; (B) Landsat 5 Thematic Mapper imagery collected on October 20, 1988, (C) burned areas in the BAMS reference data; (D) Monitoring Trends in Burn Severity perimeters; (E) Landsat Burned Area Essential Climate Variable (BAECV) classification for October 20, 1988; and (F) Landsat Burned Area (BA) classification for October 20, 1988. Omission error (OE) and commission error (CE) are shown in subfigure E and F for the BAECV and BA products, respectively.

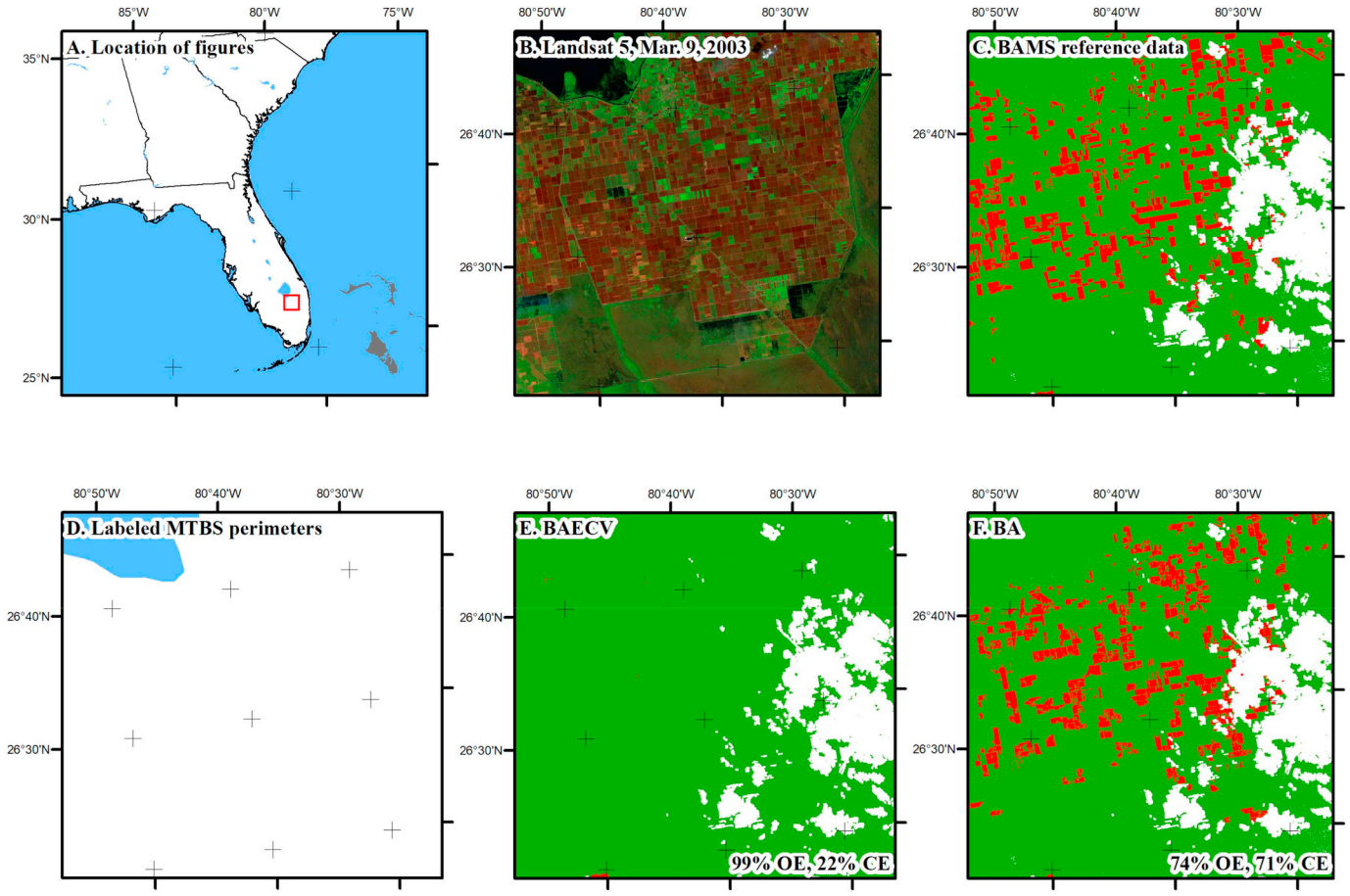

Fig. 7. Example of Landsat-based BAMS reference data with Landsat burned area products, including (A) location of figures; (B) Landsat 5 Thematic Mapper imagery collected on March 9, 2003; (C) burned areas in the BAMS reference data; (D) Monitoring Trends in Burn Severity perimeters; (E) Landsat Burned Area Essential Climate Variable (BAECV) classification for March 9, 2003; and (F) Landsat Burned Area (BA) classification for March 9, 2003. Note that the MTBS data did not contain any fires for this region. Omission error (OE) and commission error (CE) are shown in subfigure E and F for the BAECV and BA products, respectively.

Table 6
Validation statistics for the Landsat Burned Area products based on comparison with reference data derived from Landsat imagery from 1988 to 2013 for the conterminous US (CONUS) and regions of CONUS. Burned areas in cultivated crops and pasture/hay cover classes were excluded, as were burned areas mapped in prior years. Standard errors are provided in parentheses. Values show the mean of each accuracy statistic across all of the Theissen scene area polygons in CONUS used for validation (n = 28).

Exclusions	Region	Omission error (%)	Commission error (%)	Relative bias (%)
Cultivated crops, pasture/hay, prior years fires	CONUS	40 (5)	28 (2)	−17 (7.6)
	Arid West	30 (6)	27 (4)	−4 (10)
	East	61 (5)	41 (4)	−34 (9)
	Great Plains	66 (12)	33 (6)	−49 (18)
	Mountain West	41 (6)	25 (2)	−22 (8)

0.5% of all ARD scenes processed. Sometimes the excluded scenes contained legitimate burned areas, but those burned areas were usually captured in other scenes that did not have excessive commission errors. After this step, we mapped 1,219,000 km^2 in burned area from 1984 through 2018 (Fig. 9). Most places burned only once; the few places that experienced repeated burning included the Southeast, the Flint Hills in eastern Kansas, and parts of the Great Basin.

There is variability in the number of Landsat scenes collected over time (Egorov et al., 2019) and used by the BA algorithm (Fig. 10a), and care should be taken to account for this variability when assessing temporal trends in burned area. From 1984 to 1998, the TM4 and TM5 sensors were operational and collected an average of 5600 path/row scenes per year. Approximately 1% of those scenes were collected by TM4. From 2000 to 2011, when both TM5 and ETM+ were fully operational, the mean annual scene count increased to 6400 for TM, 7100 for ETM+, and 13,400 combined. After OLI/TIRS became fully operational in 2014, annual scene collection rates averaged 6600 for ETM + and 7600 for OLI/TIRS, or 14,200 combined.

In the 1984–1998 time period, burned area averaged 25,500 km^2 per year in the Landsat products (Fig. 10b). This increased in the 2000–2011 time period to 31,000 km^2/year and 31,500 km^2/year for TM and ETM+, respectively. The combined TM and ETM+ burned area averaged 41,700 km^2/year and was significantly greater than that from each sensor individually (2-sided *t*-test p-value < 0.05). In 2014–2018, OLI/TIRS mapped more burned area than ETM+ (30,400 km^2/year vs. 36,700 km^2/year; Fig. 10b) but the differences were not significant (2-sided t-test p-value = 0.15). As in the previous time period, the combined burned area (45,300 km^2/year; Fig. 10b) was significantly greater than that detected by ETM+ individually (2-sided t-test p-value < 0.01) but marginally insignificant for OLI/TIRS (2-sided t-test p-value = 0.06).

These results suggest care should be taken when using multi-sensor products to estimate rates of change or trends in burned area over time. Therefore, we assessed the temporal trends in burned area using linear regression with the TM burned area products from 1984 to 2011, ETM + products for 2012, and OLI/TIRS products for 2013–2018 (dashed grey line in Fig. 10b; Table S5). Using these data, the annual burned area averaged 30,000 km^2/year and ranged between 14,000 km^2 in

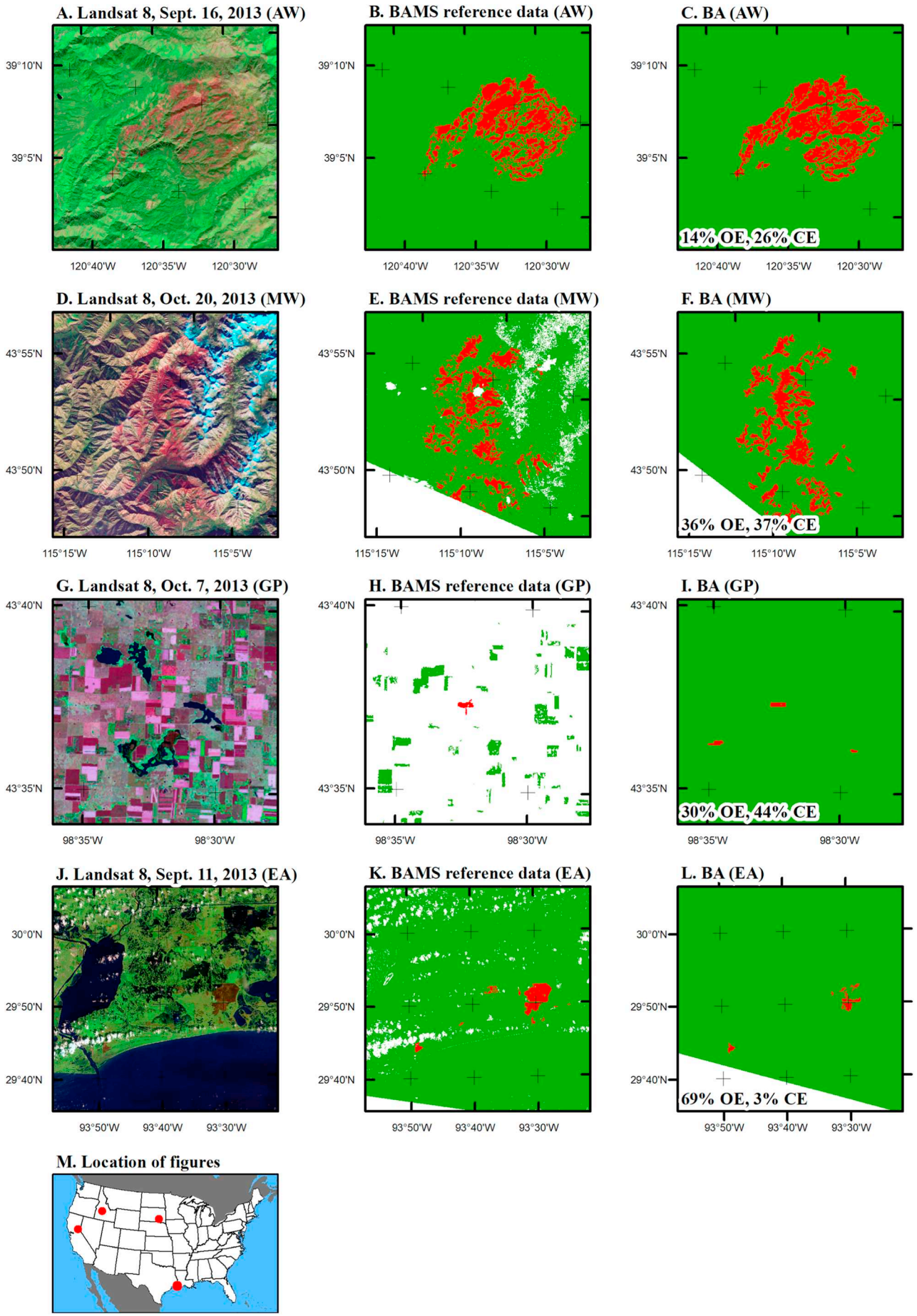

(caption on next page)

Fig. 8. Examples of imagery collected by the Landsat Operational Land Imager, corresponding BAMS reference data, and Landsat burned area (BA) burn classifications for different regions of the conterminous U.S. AW: Arid West, MW: Mountain West, GP: Great Plains, EA: East. Omission error (OE) and commission error (CE) are shown in subfigures C, F, I, and L for the BA products.

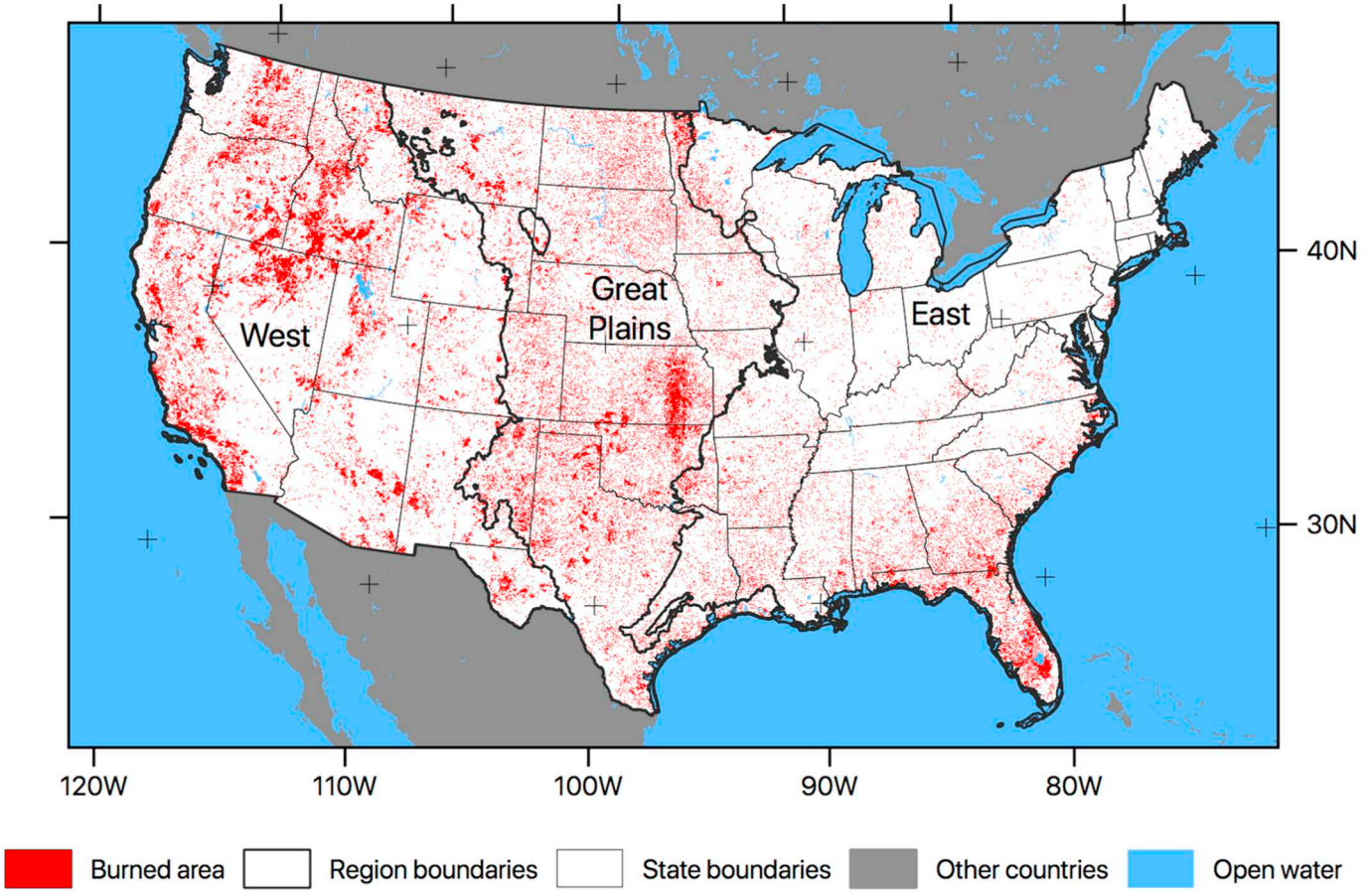

Fig. 9. All burned areas mapped at 30-m resolution across the conterminous United States from 1984 through 2018.

1991 and 46,500 km^2 in 2012. The regression fit was significant (p-value $<$ 0.01) and showed a significant increase in burned area over time (year coefficient value = 356 km^2/year, p-value = 0.01).

3.5. Differences in burned area among datasets

The BA products mapped more burned area than existing burned area datasets. Compared to the BAECV products, the BA products identified 29% more burned area per year on average from 1984 through 2015 (Fig. 11A). The greatest difference between the BAECV and BA products was in 1984 where the BA products mapped 22,800 km^2 more than the BAECV products, and 2013–2015 where the BA products mapped on average 15,000 km^2 more each year. Despite the differences in annual burned area between the BAECV and BA products, they showed similar year-to-year variability, and the linear regression relating annual burned area between the two datasets had an R^2 of 0.73 (Fig. 11B).

Annual differences between the BA products and the MTBS/GeoMAC products were more pronounced. The BA products found 183% more annual burned area than MTBS/GeoMAC products on average from 1984 through 2018 (Fig. 11C). Differences were most pronounced in 1997 when the BA products mapped nearly 18,000 km^2 more burned area than MTBS. In spite of the large differences in the amount of burned area mapped between the BA and MTBS/GeoMAC products, they also tend to show similar year-to-year variability, and the linear regression between them had an R^2 value of 0.74 (Fig. 11D).

The BA products mapped 71% more burned area annually than the MODIS MCD64A1.006 products from 2001 through 2018 (Fig. 11E). Differences between these two products were greatest in 2001 and 2002 where the BA products found 28,500 and 26,400 km^2 more burned area, respectively. The linear regression between the BA and MODIS burned area products was not as strong as it was for the BA and MTBS/GeoMAC products, with an R^2 value of 0.47 (Fig. 11F). In 2000 and 2001 only the MODIS Terra sensor was operational and not continuously, potentially influencing the results. Without those years, the relationship improved (R^2 = 0.66), and the BA product mapped 56% more annual burned area than the MODIS MCD64A1.006 products.

Spatial patterns were evident when the mean annual differences among the burned area datasets were summarized by quarter-degree quadrangles (Fig. 12). Comparing the burned area products (Fig. 12A), 78% of quarter-degree quadrangles had burned area within ± 1 km^2 of each other and 94% were within ± 3 km^2 of each other. Notable differences where the BA products mapped more burned area than the BAECV products were visible south of Lake Okeechobee in Florida, southeastern Kansas, western Minnesota, western Texas, eastern New Mexico, and scattered areas in the West. Areas where the BA products mapped less burned area than the BAECV products were in northern Florida, southern Georgia, South Dakota, northern Idaho, and northern California.

Differences at the quarter-degree scale were more pronounced for the MTBS/GeoMAC and MODIS MCD64A1.006 products (Fig. 12B and C). The BA products tended to map more burned area than the MTBS/

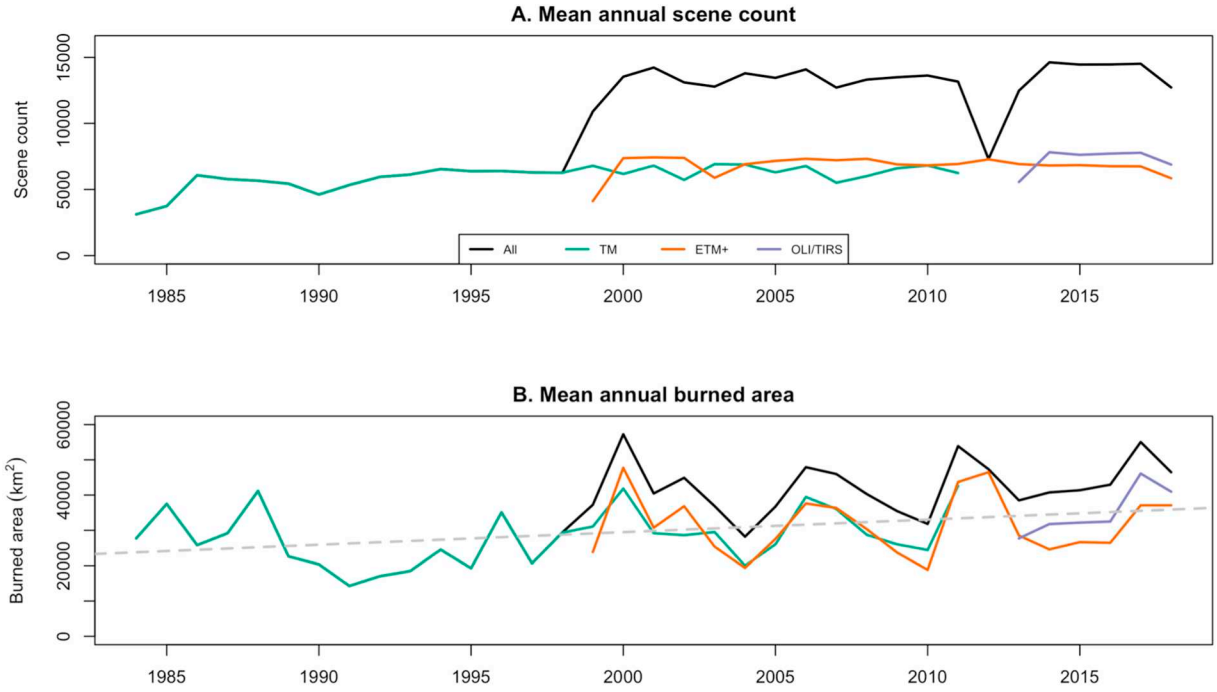

Fig. 10. Mean annual usable path/row scene count collected by each Landsat sensor and combined from 1984 to 2018 (A) and mean annual burned area in annual composites of the scene-level burned area products for each Landsat sensor and multiple sensors combined from 1984 to 2018 (B). TM: Landsat Thematic Mapper 4 and 5, ETM+: Landsat Enhanced Thematic Mapper Plus, OLI/TIRS: Landsat Operational Land Imager/Thermal Infrared Sensor. All: indicates combined results from multiple sensors (TM and ETM+ or ETM+ and OLI/TIRS). Grey dashed line shows trends in annual burned area from 1984 to 2018 fit using TM from 1984 to 2011, ETM+ for 2012, and OLI/TIRS from 2013 to 2018.

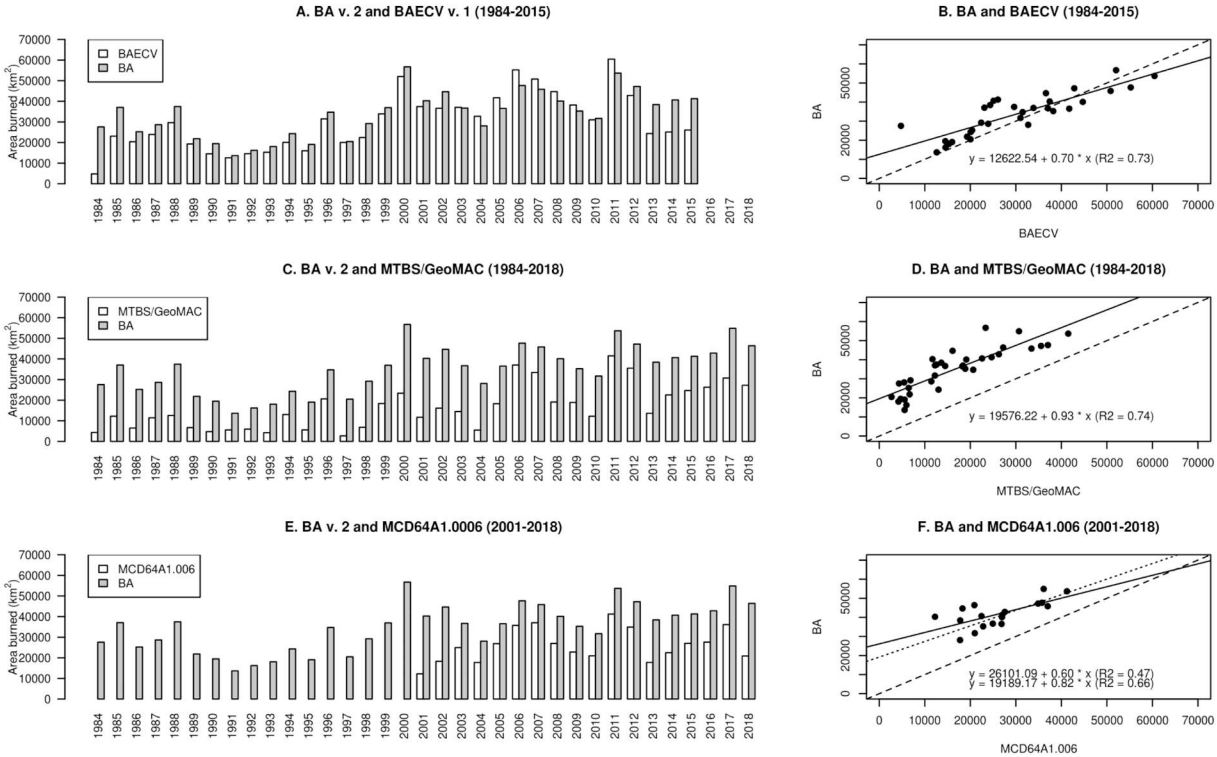

Fig. 11. Annual trends in burned area among different burned area products (BA: Landsat Burned Area products; BAECV: Landsat Burned Area Essential Climate Variable products; MTBS/GeoMAC: Monitoring Trends in Burn Severity raster layers and rasterized GeoMAC perimeters; and MCD64A1.006: MODIS burned area product, collection 6). Comparisons and correlations are made for only years where data were available for both products. Solid lines in subfigures B, D, and F represent a linear regression fit between two products; dotted line in subfigure F shows linear regression fit with 2001 and 2002 excluded in the comparison of Landsat BA and MCD64A1.006 products. 1:1 shown by dashed lines.

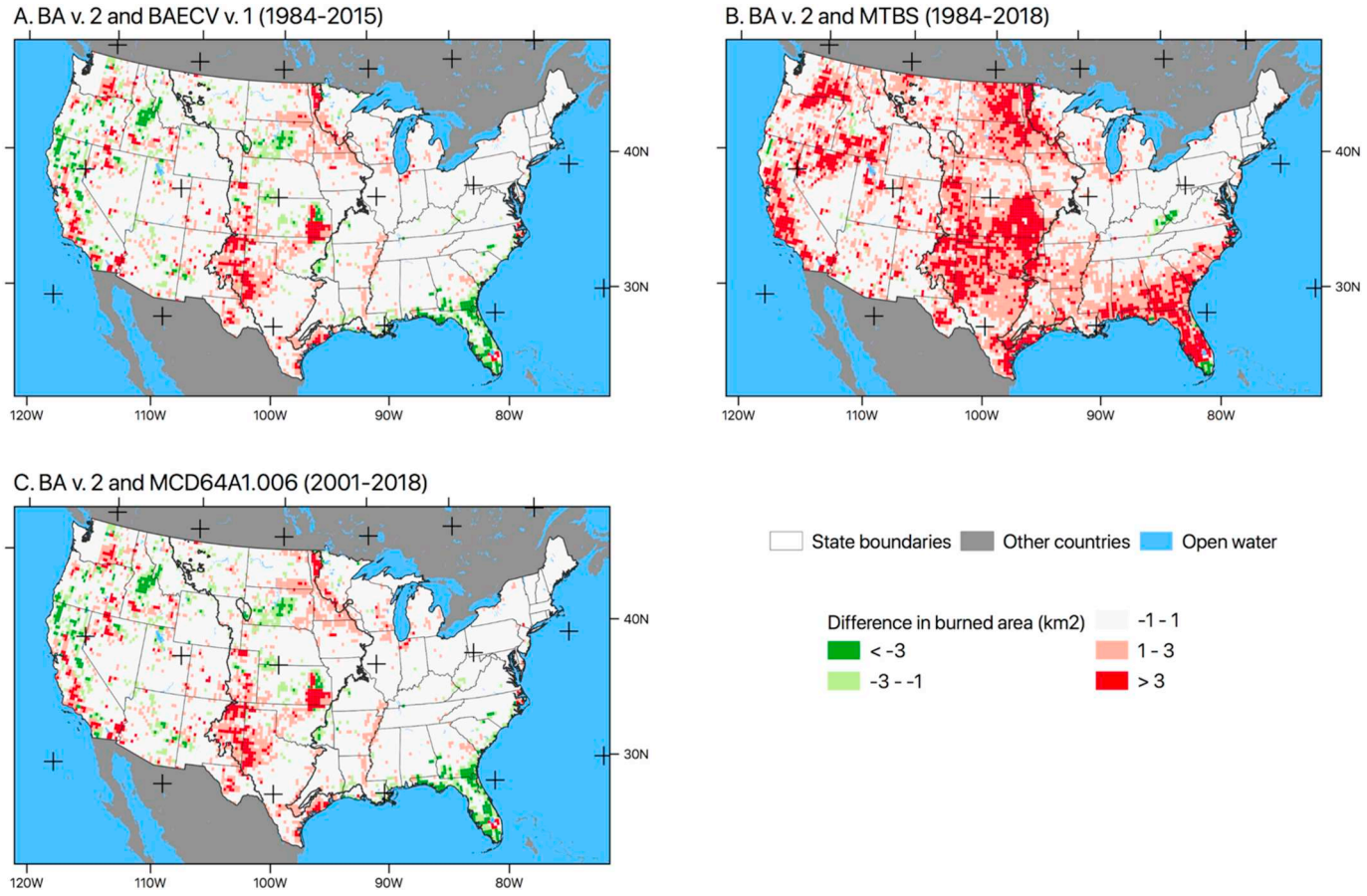

Fig. 12. Mean difference in annual burned area calculated for 1-quarter degree quadrangles between Landsat Burned Area (BA) products and (A) the Landsat Burned Area Essential Climate Variable (BAECV) products, (B) the Monitoring Trends in Burn Severity (MTBS)/GeoMAC products (1984–2018), and (C) MODIS collection six burned area products (MCD64A1.006) for 2001–2018.

GeoMAC datasets, but the differences were within 1 km^2 for 56% of quarter-degree quadrangles and within 3 km^2 for 84% of quadrangles (Fig. 12B). Differences in burned area between the BA products and MTBS/GeoMAC products were especially large across much of the Great Plains and the Southeast, California, and the Northwest, and also in the Appalachians where the BA products mapped less burned area than the MTBS/GeoMAC data (Fig. 12B).

When the BA products were compared to the MODIS MCD64A1.006 products, burned area was within ± 1 km^2 of the BA products for 57% of quarter-degree quadrangles and within 3 km^2 for 84% of the quadrangles (Fig. 12C). The MODIS data showed more burned area in the Mississippi River Valley and southern Florida. However, the BA products tended to map more burned area across much of the country, following similar patterns as the MTBS data but with more pronounced differences in the western US.

The Flint Hills of eastern Kansas offer an example of where differences in burned area among the datasets were especially large. Closeups of the differences and original data showed that all three datasets mapped similar patterns of burned area in grassland land-cover types (Fig. 13); however, the BA products mapped more burned area with finer detail. Additional differences were visible in cultivated crop cover types where the MCD64A1.006 product mapped greater amounts of burned area and the MTBS products mapped no burned area.

3.6. Differences in date of detection among datasets

We calculated the mean annual reported date of burn detection for each product (Landsat BA, FPA-FOD, and MCD14ML.006) by quarter-degree quadrangles. We assumed that burned areas mapped by the BA algorithm before the FPA-FOD fires and MCD14ML.006 active fire detections were FPA-FOD or MCD14ML omission errors or BA commission errors and excluded them from the date comparison. In quarter-degree quadrangles where the BA products mapped burned areas after the FPA-FOD fires and MCD14ML.006 active fire detections, we calculated the annual difference in the mean of detection dates among datasets. The annual differences were then averaged for each quarter-degree quadrangle. The differences were grouped into 16-day intervals, corresponding to the interval between overpass dates for each Landsat sensor (Fig. 14). We then compared datasets in terms of the cumulative percentage of quarter-degree quadrangles that had date differences less than or equal to each 16-day interval.

Differences in detection dates were similar among the Landsat BA, FPA-FOD, and MCD14ML.006 products. The percentage of quarter-degree quadrangles with mean date difference of 16 days was 15% for the FPA-FOD data and 18% for the MCD14ML.006 data. However, as the temporal interval increased, so did the percentage of quarter-degree quadrangles with date differences within the interval. For instance, the percentage of quarter-degree quadrangles increased to 70% and 76% for the FPA-FOD and MCD14ML.006 data, respectively, for 64-day or less date differences; 96% and 97% of quadrangles had 128-day or less date differences for the FPA-FOD and MCD14ML.006 data, respectively (Fig. S2). The difference in detection date represents both the lag in detection of burned areas because of the 16-day time span between Landsat overpass interval and cloud cover, and in the case of the FPA-FOD, the differences between the reported ignition date and the rates of fire spread. Spatial agreement in detection dates appeared to be greater in the western US and lower in the eastern US where cloud-cover could influence image availability (Fig. 14).

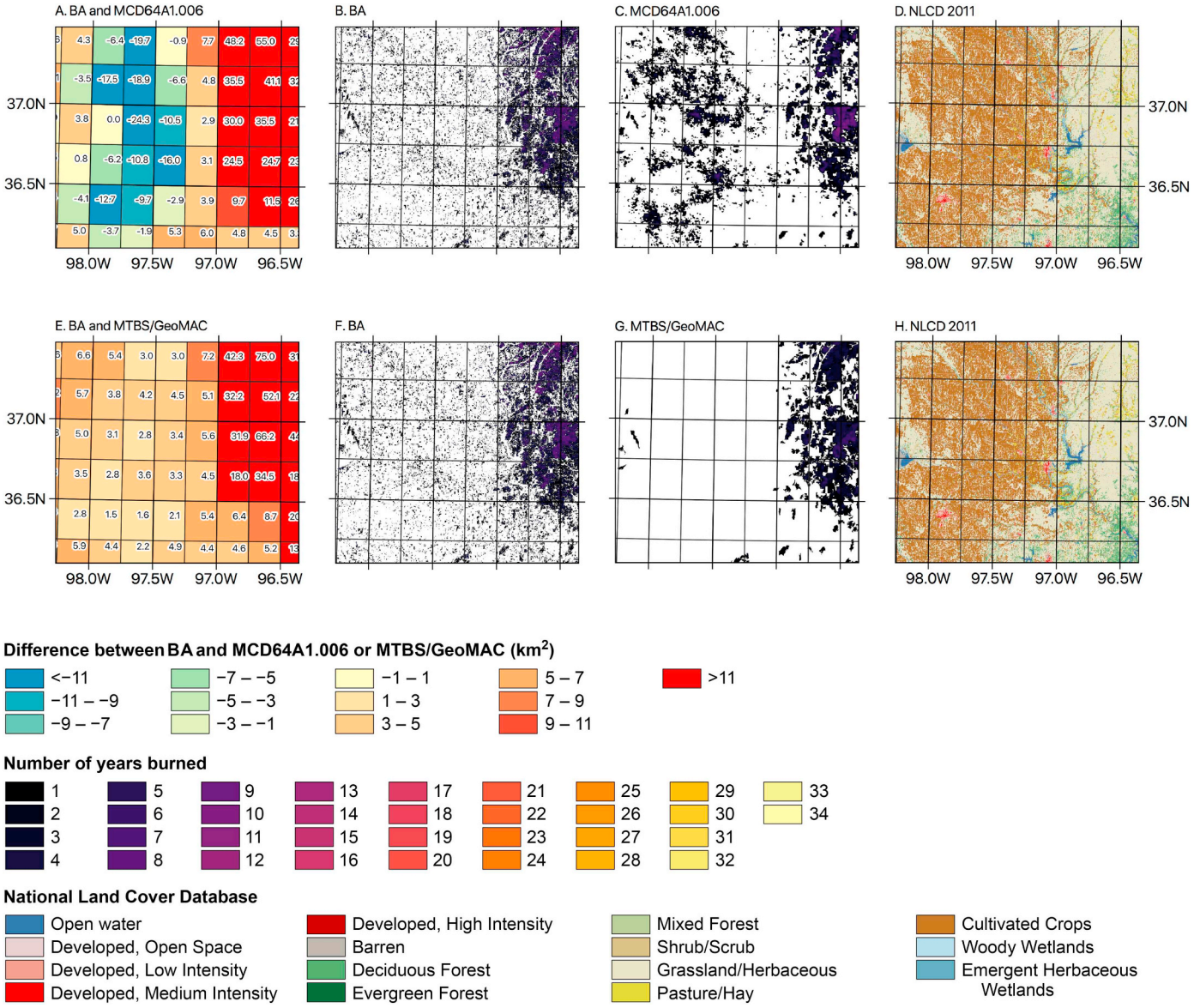

Fig. 13. Closeups showing differences between data products. Labels in subfigure A indicate difference between the Landsat Burned Area (BA) and MCD64A1.006 in km^2 for 2001–2018 (subfigures A–D) and differences between the BA products and the combined Monitoring Trends in Burn Severity (MTBS) and GeoMAC products for 1984–2018 (subfigures E–H). Counts of the number of years a pixel was mapped as burned are shown in subfigures B, C, and F, and G for the different datasets. The 2011 National Land Cover Database layer is shown in subfigures D and H for reference.

4. Discussion

We developed the Landsat BA algorithm to map burned areas across the CONUS and produce new 30-m burned area products from 1984 through 2018. The BA products supersede the BAECV products and are unique in that they are the longest-running record of burned area for the CONUS collected over the length of the Landsat archive, whereas other existing data sources have a more limited time span (e.g. MCD64A1) or rely on agencies' records which have spatiotemporal variability in reporting effort (Brown et al., 2002; Eidenshink et al., 2007; Fusco et al., 2019; Short, 2015). Consequently, the BA products identified 1,219,000 km^2 of burned area from 1984 through 2018 and tend to map more burned area than existing products: 29% more than BAECV (1984–2015), 183% more than MTBS/GeoMAC (1984–2018), and 56% more than MODIS MCD64A1.006 (2003–2018). The differences are because the BA products include burned areas in agricultural areas (23% of all burned areas) and map small fires and fires not present in the other data sources. The BA products also map fires with greater spatial detail than other burned area products. In spite of the differences among products, they tend to map similar patterns of year-to-year variability in burned area, especially between the BA and BAECV products, and MTBS/GeoMAC products, and to a lesser extent with the MCD64A1.006 products.

The amount of burned area detected by the Landsat burned area algorithm varies in relation to the number of Landsat images collected in different time periods. Less than half as many images are available in the archive prior to 1999 when only the TM sensors were operational (Egorov et al., 2019). After 2002, the Landsat 7's scan-line corrector (SLC) error introduces gaps in images collected (Kovalskyy and Roy, 2013) which could also reduce the amount of burned area detected. Because burned areas are persistently visible in many regions, the increased collection effort did not result in an equivalent increase in detected burned area. From 2000 through 2011, the addition of ETM+ increased the annual count of scenes collected by 139% over those collected by TM from 1984 through 1998. However, mean annual burned area increased by 64% between the same time periods. Some,

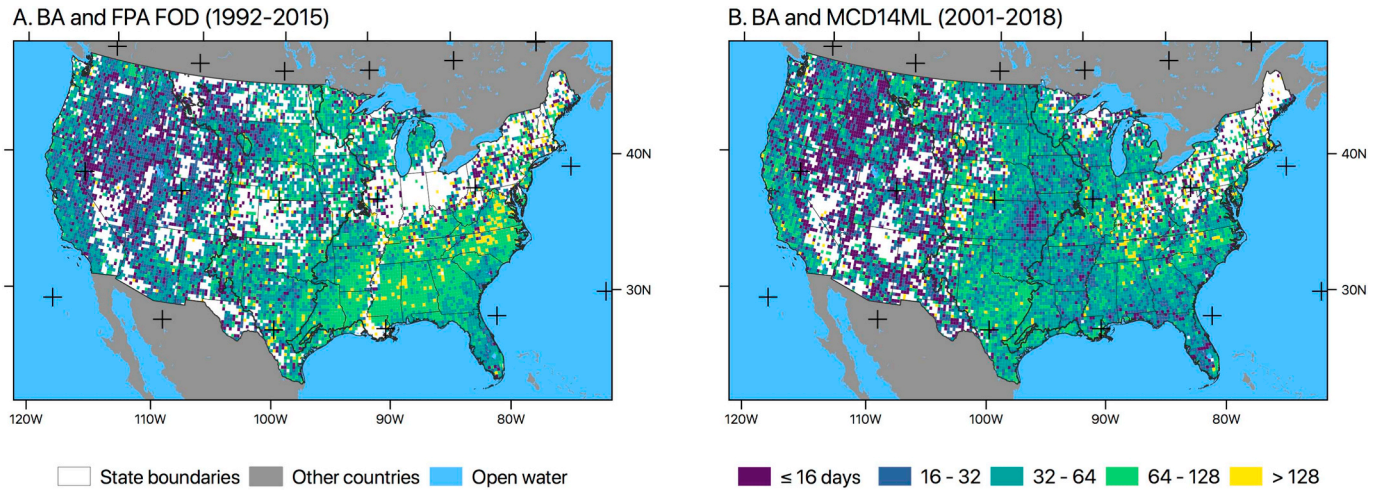

Fig. 14. Mean of annual differences in date of detection for each quarter-degree quadrangle between (A) the Landsat Burned Area (BA) products and the Fire Program Analysis (FPA) fire occurrence database (FOD) from 1992 through 2015 and (B) the Landsat Burned Area products and the MODIS MCD14ML active fire detections from 2001 through 2018.

but not all, of this change was attributable to the increase in scene collection effort. For example, from 2000 to 2011 the burned area detected by ETM+ and TM combined was 35% greater than TM alone. From 2014 through 2018, burned area detected by OLI/TIRS alone was 21% greater than ETM+ alone, in part documenting the influence of the SLC error but also possibly documenting the higher radiometric resolution and more narrow spectral bands of OLI/TIRS (Roy et al., 2016). In that same time period, 49% more burned area was detected by ETM+ and OLI/TIRS combined than ETM+ alone. Investigating the influence of collection effort on burned area detection suggests that the Landsat burned area products provide conservative estimates of burned area prior to 2000 when most of the scenes were collected by TM. The limitations of reduced collection effort, whether from having only TM imagery or from the SLC error may be especially pronounced in areas where cloud cover and rapid vegetation regrowth reduce the duration over which burned areas remain visible such as the Southeast and Great Plains and less important in other regions like the West and upper Great Lakes where burned areas remain visible for months to years.

Given the influence of collection effort on the amount of burned area mapped, use of the burned area products combined across Landsat sensors would be appropriate when users require the best estimate of total burned area for an individual fire or region. For analyzing trends in burned area, combining data from multiple sensors may be appropriate after 2000 when all years except 2012 had 2 operational Landsat sensors. However, analyzing trends in burned area over the length of the archive (1984–2018) requires controlling for variability in collection effort. One option is to use burned area products from individual sensors instead of the combined products. Our results using this approach document significant increases in annual burned area over time. This finding is supported by previous studies that also document increases in burned area over the time period of this study using both remote sensing products and agency fire records (Westerling, 2011; Dennison et al., 2014; Picotte et al., 2016; Abatzoglou and Williams, 2016; Balch et al., 2017).

Based on extensive visual analysis of the Landsat burned area products, regression analysis of trends in burned area over time, high correlations in annual burned area with the MTBS/GeoMAC and MCD64A1.006 products, and reasonable error estimates based on validation with reference data derived from both Landsat and high-resolution imagery, we have confidence that the BA data are representing realistic patterns of burning. Thus, the new BA products provide a unique data source to monitor and assess spatial and temporal patterns of burning with 30-m resolution and will continue to do so into the future as they are routinely updated as new Landsat data are collected. Latency for the burned area products is approximately 25–27 days for ETM+ data and 15–17 days for OLI/TIRS data.

4.1. Validation

The preferred approach to validating remote sensing data products has been to use reference data derived from imagery with higher spatial resolution than the data products (Boschetti et al., 2016; Padilla et al., 2015; Roy et al., 2005; Vanderhoof et al., 2017a); however, this is difficult to accomplish when validating Landsat products (Vanderhoof et al., 2017b). High-resolution images have not been routinely collected over the entire temporal extent of the Landsat archive and that limits the use of statistical sampling designs for validation. Consequently, our validation results from high-resolution imagery may not be representative of the entire spatial and temporal extent covered by our data products. For instance, a different sampling strategy focused on more heavily sampling low-frequency fire areas could have modified our estimates of commission error. In spite of these limitations, validation with high-resolution reference data can be used to compare product versions and we found that the changes we made to the BA algorithm resulted in the BA products having lower omission and commission error rates than the BAECV products.

Because of the limitations of validating Landsat products with high-resolution commercial satellite imagery, we also validated the products with reference data derived from Landsat imagery. This showed minimal increases in omission error (2% increase) and substantial increases in commission error (11% increase) over the BAECV products (Table 4; Vanderhoof et al., 2017b). However, the increase in commission error was almost entirely attributable to an increase in the amount of area the BA products identified as burned in cultivated crops and pasture/hay land-cover classes. In contrast, the Landsat-based reference dataset is acknowledged to underestimate burned area in these cover types. When burned areas in cultivated crops and pasture/hay land-cover classes were excluded, the BA products showed a 2% decline in commission error relative to the BAECV products across the remaining cover types. This is comparable to the 7% decline in commission error observed using the high-resolution reference dataset across all cover types. Successfully separating burned areas in agricultural land-cover classes is a problem common to many burned area products (Giglio et al., 2016; Long et al., 2019) and this problem affects both the BA and BAECV products, as well as the validation data derived from Landsat imagery. We suspect the greater commission error in these classes is a result of reducing the number of predictor variables used in the BA algorithm to 8 instead of the 43 predictors used by the

BAECV algorithm. In spite of the increased error rates in cultivated crops and pasture/hay land-cover classes, we were impressed that the reduction in predictors had minimal impact on algorithm performance in wildland vegetation types (forest, shrub, grassland, wetlands). Considering the processing performance gains made by reducing the number of predictors, sacrificing accuracy in these land-cover classes seemed a reasonable tradeoff.

Commission error was further reduced by 2% by adding a processing step to remove burned areas that overlapped burned areas mapped in previous years. This is unique to our algorithm because other approaches to mapping burned areas with Landsat data have relied on short-term summaries for reference conditions that likely included changes from previous fires. For instance, Boschetti et al. (2015) used weekly differences between Landsat images, Roy et al. (2019) used scene-to-scene differences, and Long et al. (2019) used 1-year summaries of reference conditions. Methods using other sensors have also made use of short intervals between images to circumvent this problem (Giglio et al., 2018; Roteta et al., 2019). For our approach, the 3-year reference window was important for early years in the Landsat archive when fewer images were available and also to limit year-to-year variability in vegetation conditions (e.g. drought) that might cause confusion when detecting burned areas. Other burned area mapping algorithms that span the entire Landsat archive have made use of both short- and long-term historical summaries. For example, Goodwin and Collett (2014) used the preceding seven images dates and seasonal medians from images collected within 5 years as predictors in their algorithm.

Overall, our validation results indicated that performance of the BA algorithm is quite good, and commission and omission error rates were 28% and 40%, respectively, when validated with Landsat-derived reference data and 19% and 41%, respectively, when validated with high-resolution commercial satellite imagery. The nearest comparable burned area product for CONUS is the MTBS data. The primary limitation is that MTBS doesn't map all fires, only large fires that are reported in federal databases (Eidenshink et al., 2007) and because they focus on large fires reported by agencies, the MTBS data are likely biased (Brown et al., 2002; Fusco et al., 2019; Hawbaker et al., 2008; Short, 2015). Therefore, we compare the accuracy of the BA products to other global burned area products. As with the BAECV products, our error rates were lower than many global, coarse-resolution products which have commission errors ranging between 42 and 94% and omission errors ranging between 68 and 93% (Padilla et al., 2015). Global Landsat burned area products recently produced for 2015 in Google Earth Engine (Long et al., 2019) had lower commission and omission error rates (13% and 30%, respectively) than our products. However, actual error rates are uncertain because Long et al. (2019) appear to have validated their products over the US with MTBS data and the MTBS data do not include all burned areas.

4.2. Lessons learned

The BA algorithm is an extensive update from the BAECV algorithm, and there were some important lessons learned during the process. Compared to the BAECV algorithm which used Landsat data in the native path/row format, the BA algorithm was designed to accommodate the new ARD format. This format was intended to reduce preprocessing and make it easier for users to produce derived products by consistently tiling, georegistering, atmospherically correcting, and assessing the quality of Landsat data (Dwyer et al., 2018). Similar efforts have been made in other countries to standardize Landsat data delivery such as the Australian Earth Observation Data Cube (Lewis et al., 2015). Refining our approach to accommodate the ARD format was also necessary to incorporate OLI/TIRS data. Including these data allowed us to bring our burned area products up to date (through 2018) and also positioned the USGS for forward processing of burned area products beyond 2018 as both ETM+ and OLI/TIRS data are collected into the future. The L1TP ARD data are considered to have the highest available quality and are most suitable for time-series analysis (Dwyer et al., 2018). Early adopters of the Landsat ARD data have documented greater change-detection accuracies when using ARD data compared to path/row data (Zhu et al., 2019). Although we did not assess whether or not the ARD format improved our results over the path/row format, we did find that the tiled imagery in the ARD format reduced preprocessing time and facilitated generation of historical reference and change predictors, as well as, annual composites of the BA products. In spite of the reduced preprocessing requirements and other processing efficiencies provided by the ARD format, the increased data volume required us to eliminate other processing bottlenecks in our algorithm to make processing burned area products from the Landsat archive for CONUS feasible. For example, across CONUS from 1984 through 2018, there were an average of 475 images per path/row. For the same region and time period, the ARD tiles include an average of 2094 images per tile, a 340% increase. Furthermore, the rate of image collection is increasing for both ETM+ and OLI/TIRS (Wulder et al., 2019). Changes were needed to reduce the time our algorithm required to process the greater volume of imagery.

Initial testing found that the GBRM used to generate the burn probability surfaces was a significant bottleneck in processing. Reducing the number of trees, splits per tree, and predictor variables used are potential approaches to reducing GBRM processing time. Thus, we initially optimized the number of trees and splits per tree, and then sought to improve processing performance by implementing a forward selection procedure to reduce the number of predictor variables. We tested a large suite of 68 potential predictor variables during the process of developing the BA algorithm. The spectral indices were designed to monitor vegetation vigor and water content (EVI, NBR, NBR2, NDMI, NDWI, NDVI, SAVI, VI43, VI45, and VI57), enhance the charcoal and ash signal (BAI, CSI, and MIRBI), or to incorporate the thermal band (NBRT1, VI6T, and VI46); and previous studies have shown them to be effective at mapping both burned area and burn severity (Table 2).

Past studies using remote sensing to map burned area over large spatial extents selected spectral indices and predictors based on findings in previous publications or the authors' understanding of which predictors work well in their region of interest (Alonso-Canas and Chuvieco, 2015; Boschetti et al., 2015; Giglio et al., 2018; Goodwin and Collett, 2014; Hawbaker et al., 2017; Long et al., 2019; Roteta et al., 2019). Many of these past efforts have included multiple spectral indices to utilize the unique characteristics of each index. Also, the ability of any single spectral index to separate burned from unburned areas varies among ecosystem type and burn severity (Tran et al., 2018) and change-detection methods are generally more successful when using multiple spectral indices (Cohen et al., 2018; Zhu et al., 2019). Whether past studies have selected the most effective predictors is unclear, especially when their interactions are considered. Thus, variable or feature selection can be a critical step to identify the most relevant predictors while at the same time reducing the computational demand of calculating all potential predictors. This was what Ramo et al. (2018) found when they used random forest, entropy-based filtering, and logistic regression models to reduce a set of 52 potential predictors down to 8 for mapping burned areas with MODIS spectral and hotspot data. Our forward selection procedure also selected 8 predictors but from a larger set of 68 potential predictors, greatly reducing the amount of time required to calculate spectral indices, historical summaries, and change metrics used by the GBRM.

Our results and those of Ramo et al. (2018) suggest that at some point there may be a limit to the accuracy gains that additional pixel-level predictors provide. To move beyond that limit, other types of information might be required. Such information could be provided by hybrid algorithms incorporating both burned area detection and hotspots (Alonso-Canas and Chuvieco, 2015; Fraser et al., 2000; Giglio et al., 2009). The hybrid approach has been demonstrated using Landsat and MODIS hotspots by Boschetti et al. (2015). However,

differences in temporal and spatial resolution make use of MODIS hotspots with Landsat burned area detection challenging. Furthermore, the revisit intervals of the Landsat satellites will likely prevent effective use of Landsat hotspots (Schroeder et al., 2016) for improving burned area detection. Alternative approaches include combining imagery from multiple sensors (Roy et al., 2019), adopting regionally sensitive approaches (Roteta et al., 2019) or more sophisticated time-series analysis (Huang et al., 2010; Kennedy et al., 2010; Verbesselt et al., 2010; Zhu and Woodcock, 2014a), or use of change-detection methods that incorporate both spatial patterns as well as temporal trends and may be less sensitive to temporal noise (Boschetti et al., 2015; Giglio et al., 2018; Goodwin and Collett, 2014; Ludwig et al., 2017).

The predictor variables selected for use in the GBRM included the scene-level NBRT1, VI6T, VI45, NDVI, the 3-year lagged mean of NBRT1, VI45, and NDVI, and the 3-year standard deviation of NBRT1 (Fig. 3). These predictors make use of the red, NIR, SWIR1, SWIR2, and thermal bands; predictors relying on these bands have repeatedly been shown to be effective for mapping burned area and severity (Chuvieco et al., 2002; Chuvieco and Congalton, 1988; García and Caselles, 1991; Holden et al., 2005; Huang et al., 2016; Key and Benson, 2006; Ramo et al., 2018; Tran et al., 2018; Trigg and Flasse, 2000; van Wagtendonk et al., 2004). Selection of predictors using the thermal band (NBRT1 and VI6T) was not surprising given that the thermal band was the most important predictor in the BAECV algorithm (Hawbaker et al., 2017) and past studies have found that spectral indices incorporating thermal information often have higher separability for burned areas than indices that do not (Harris et al., 2011; Holden et al., 2005). However, indices based entirely on spectral data are more widely used than indices incorporating thermal data. The more typical approach is to use thermal hotspots to separate burned areas from other types of land change (Alonso-Canas and Chuvieco, 2015; Boschetti et al., 2015; Giglio et al., 2018; Roteta et al., 2019). Until recently, there was not a standard method to generate consistent land-surface temperature values and consequently the Landsat thermal bands have been underutilized in large-scale mapping efforts (Malakar et al., 2018; Wulder et al., 2019). Reliance of the BA algorithm on the TOA brightness temperature values may be problematic and could have contributed to the classification artifacts that remained. However, the demonstrated importance of the thermal band in the BAECV algorithm and the BA algorithm highlight the potential utility of standardized surface temperature products (Malakar et al., 2018) for identifying burned areas in future products.

Scene-level and reference predictors were chosen over change predictors by our selection process. This was by design as we tested scene-level spectral indices for inclusion first and tested the reference variables (3-year lagged mean and standard deviation) and the change predictor for a given spectral index for inclusion only after the scene-level predictor was selected. This decision was designed to favor scene-level predictors, which are more computationally inexpensive to calculate compared to the reference and change predictors. The initial favoring of scene-level predictors is justified because past approaches for mapping burned area and severity have found that they can work quite well (Eidenshink et al., 2007; Koutsias and Karteris, 2000; Long et al., 2019). However, we were surprised that no change predictors were selected given their extensive use in other approaches to map burned area (Alonso-Canas and Chuvieco, 2015; Boschetti et al., 2015; Giglio et al., 2018; Goodwin and Collett, 2014; Key and Benson, 2006; Koutsias and Karteris, 1998; Ramo et al., 2018; Roteta et al., 2019; Roy et al., 2019). Many of those same studies also use predictors characterizing pre-fire reference conditions which can be important to separate burnable land-cover types from unburnable land-cover types. We do not suggest that change predictors are not useful, but our findings do suggest that identifying burned areas can be successful when both pre-fire and post-fire conditions are characterized individually as an alternative to relying on change metrics.

Spectral differences between Landsat TM, ETM+, and OLI data have been previously documented (Roy et al., 2016; Steven et al., 2003). One might expect that such differences would influence the success of change and disturbance detection algorithms. We did not find that to be the case for detecting burned areas; initial testing of our GBRM model included a variable indicating from which sensor an image was collected, but it did not improve our GBRM fit enough to be included by our forward selection procedure. A sensor predictor was included in the BAECV algorithm, but had low relative importance compared to other predictors (Hawbaker et al., 2017). Based on those results, we suggest that the spectral variability among sensors is minimal compared to the spectral changes induced by fires.

In spite of the increased performance of the BA algorithm, visually assessing the results was necessary to identify and remove images with excessive commission errors. As part of our processing pipeline, graphics were generated for each individual Landsat scene and the associated burned area products. These graphics were instrumental in efficiently visualizing the thousands of scene-level products our algorithm generated and quickly identifying troublesome scenes. However, they also highlighted one tradeoff that comes with the ARD format–it can be challenging to track specific areas within the ARD tile when there are gaps in overlap between ARD scenes. This step emphasizes that in addition to generating quantitative validation metrics, data visualization remains an essential step to remote sensing product development but has become increasingly challenging given the volume of data that is now available and can be quickly processed using cloud computing (Gorelick et al., 2017).

Documenting fire activity at national scales is difficult and in spite of improvements in databases used for reporting fires, they are still prone to human error and inconsistent reporting effort. Additionally, even when fire information is correctly entered into databases, it may not fully represent fire impacts. For instance, fire perimeters may not include unburned areas within a fire perimeter (Kolden and Weisberg, 2007; Meddens et al., 2016). Remote sensing offers promise here; however, critical differences remain between agency records and remotely sensed burned area products. A good example is the MTBS data which combine perimeters and severity information derived from remotely sensed data with attributes from agency records. Those attributes are often critical for understanding and modeling patterns of fire occurrence and fire impacts (Abatzoglou et al., 2017; Abatzoglou and Williams, 2016; Balch et al., 2017; French et al., 2014; Picotte et al., 2016; Urbanski et al., 2018). Recent developments offer promise to improve these shortcomings using remote sensing. For example, the recently produced fire atlas identifies individual fires in the MCD64A1.006 burned area data and attributes them with information about timing, duration, fire speed, and direction (Andela et al., 2018). Improving attribution of burned area products could also be accomplished by joining agency fire incident reports with remotely sensed burned area products; however, mismatches in the spatial locations and timing of the different fire data may make such an effort challenging (Fusco et al., 2019; Hawbaker et al., 2008), especially in areas where prescribed fire is common (Nowell et al., 2018). We are optimistic that these challenges will eventually be overcome in the future as more and more sensors, such as Sentinel-2 that are capable of mapping active fires and burned areas become operational and provide records of fire activity with greater temporal frequency and spatial resolution than we currently have (Frantz, 2019; Moran et al., 2019; Roteta et al., 2019; Roy et al., 2019; Verhegghen et al., 2016; Wulder et al., 2019). However, attribution of historical burned area products will likely remain limited to manual efforts to reconcile the spatial and temporal differences among the datasets available.

5. Conclusions

Changes made to the Landsat BA algorithm from the BAECV algorithm to handle the increased data volume of the ARD stacks and to incorporate OLI/TIRS data improved the error rates of the resulting

products. These products excel at consistently mapping burned areas 2 ha and larger over time and across CONUS while capturing within-fire heterogeneity. Such characteristics are critical for understanding long-term impacts of fire on human and natural systems. The differences between the Landsat BA, BAECV, MTBS/GeoMAC, and MCD64 products highlight the unique information that Landsat-derived burned area products can add, especially in terms of spatial detail and the time span of fire history they offer. The differences in burned area we found have implications for understanding patterns of fire occurrence and fire impacts (Abatzoglou and Williams, 2016; French et al., 2014; Ghimire et al., 2012; Picotte et al., 2016; Radeloff et al., 2018; Sankey et al., 2017; Shakesby and Doerr, 2006; Urbanski et al., 2018). Our BA products and the suite of remotely sensed fire products being produced by others (Chuvieco et al., 2019) demonstrate the utility remote sensing offers for continuous earth surface monitoring.

6. Data and source code access

The Landsat BA products are part of the suite of Level-3 Science Products now being produced for the Landsat archive. Currently, Dynamic Surface Water Extent (Jones, 2015, 2019) and Fractional Snow-Covered Area (Selkowitz and Forster, 2016) are produced in addition to the burned area products. All Level-3 Science Products are available for download from USGS's EarthExplorer (https://earthexplorer.usgs.gov). Scene-level BA products are described in detail at https://doi.org/10.5066/F77W6BDJ; BA data are available through EarthExplorer and will be processed periodically as new Landsat data are collected. The burned area validation data are available for download from Vanderhoof et al. (2020; doi.org/10.5066/P9QKHKTQ). Annual composites, generated from the scene-level BA products, are available for download from Hawbaker et al. (2020; doi.org/10.5066/P9QKHKTQ) and https://gec.cr.usgs.gov/outgoing/baecv/LBA/LBA_CU_C01_V01 Source code for the Landsat Burned Area algorithm can be found at https://github.com/USGS-EROS/espa-burned-area/tree/burned_area_v1.2.0

CRediT authorship contribution statement

Todd J. Hawbaker: Conceptualization, Methodology, Software, Formal analysis, Resources, Data curation, Writing - original draft, Writing - review & editing, Visualization, Supervision, Project administration, Funding acquisition. **Melanie K. Vanderhoof:** Conceptualization, Methodology, Validation, Formal analysis, Data curation, Writing - original draft, Writing - review & editing, Visualization, Supervision, Project administration, Funding acquisition. **Gail L. Schmidt:** Methodology, Software, Data curation, Writing - review & editing. **Yen-Ju Beal:** Methodology, Software, Validation, Formal analysis, Data curation, Writing - review & editing, Visualization. **Joshua J. Picotte:** Conceptualization, Writing - original draft, Writing - review & editing. **Joshua D. Takacs:** Methodology, Software, Resources, Writing - review & editing. **Jeff T. Falgout:** Methodology, Software, Resources, Writing - review & editing. **John L. Dwyer:** Conceptualization, Resources, Data curation, Writing - review & editing, Supervision, Project administration, Funding acquisition.

Declaration of competing interest

The authors declare that they have no known competing financial interests or personal relationships that could have appeared to influence the work reported in this paper.

Acknowledgements

Funding for this work was provided by the U.S. Geological Survey's Land Resources Mission Area through the National Land Imaging Program and Land Change Science Program. Products were generated on the Yeti high-performance computing cluster with assistance from the Advanced Research Computing group in the Science Analytics and Synthesis Program of the US Geological Survey's Core Science Systems Mission Area. Jeremy Havens helped create figures presented in the manuscript. Calli Jenkerson and Christopher Barnes helped with project management and communications; both are contractors to the U.S. Geological Survey, Earth Resources Observation and Science Center through KBR. We appreciate feedback on initial products and suggestions for product formats from Casey Teske and Joe Nobel at Tall Timbers Research Station and Land Conservancy and team members from the Monitoring Trends in Burn Severity and LANDFIRE projects. Finally, we are grateful to the Editor and three anonymous reviewers for Remote Sensing of Environment, as well as Christopher Soulard, R. Randall Schumann, Harland Goldstein, and Janet Slate for providing comments and suggestions on previous versions of this manuscript. Any use of trade, firm, or product names is for descriptive purposes only and does not imply endorsement by the U.S. Government.

Appendix A. Supplementary data

Supplementary material to this article can be found online at https://doi.org/10.1016/j.rse.2020.111801.

References

Abatzoglou, J.T., Kolden, C.A., 2013. Relationships between climate and macroscale area burned in the western United States. Int. J. Wildland Fire. https://doi.org/10.1071/wf13019.

Abatzoglou, J.T., Williams, P.A., 2016. Impact of anthropogenic climate change on wildfire across western US forests. Proc. Natl. Acad. Sci. 113, 11770–11775. https://doi.org/10.1073/pnas.1607171113.

Abatzoglou, J.T., Kolden, C.A., Williams, P.A., Lutz, J.A., Smith, A., 2017. Climatic influences on interannual variability in regional burn severity across western US forests. Int. J. Wildland Fire. https://doi.org/10.1071/WF16165.

Adler-Golden, S.M., Berk, A., Bernstein, L.S., Richtsmeir, S., Acharyal, P.K., Matthew, M.W., Anderson, G.P., Allred, C.L., Jeong, L.S., Chetwynd, J.H., 1998. FLAASH, a MODTRAN4 atmospheric correction package for hyperspectral data retrievals and simulations. In: Proceedings of the Summaries of the Seventh JPL Airborne Earth Science Workshop, Pasadena, CA, USA, 12–16 January 1998, pp. 1–6.

Adler-Golden, S.M., Matthew, M.W., Bernstein, L.S., Levine, R.Y., Berk, A., Richtsmeier, S.C., Acharya, P.K., Anderson, G.P., Felde, J.W., Gardner, J.A., Hoke, M.L., Jeong, L.S., Pukall, B., Ratkowski, A.J., Burke, H.K., 1999. Atmospheric correction for shortwave spectral imagery based on MODTRAN4. In: SPIE Proceedings. Imaging Spectrometry.

Alonso-Canas, I., Chuvieco, E., 2015. Global burned area mapping from ENVISAT-MERIS and MODIS active fire data. Remote Sens. Environ. 163, 140–152. https://doi.org/10.1016/j.rse.2015.03.011.

Andela, N., Morton, D.C., Giglio, L., Paugam, R., Chen, Y., Hantson, S., van der Werf, G.R., Randerson, J.T., 2018. The Global Fire Atlas of individual fire size, duration, speed, and direction. Earth System Science Data Discussions 1–28. https://doi.org/10.5194/essd-2018-89.

Balch, J.K., Bradley, B.A., Abatzoglou, J.T., Nagy, C.R., Fusco, E.J., Mahood, A.L., 2017. Human-started wildfires expand the fire niche across the United States. Proc. Natl. Acad. Sci. 114, 2946–2951. https://doi.org/10.1073/pnas.1617394114.

Bastarrika, A., Alvarado, M., Artano, K., Martinez, M., Mesanza, A., Torre, L., Ramo, R., Chuvieco, E., 2014. BAMS: a tool for supervised burned area mapping using Landsat data. Remote Sens. 6, 12360–12380. https://doi.org/10.3390/rs61212360.

Boschetti, L., Roy, D., Justice, C., 2009. International global burned area satellite product validation protocol. In: Cal Val, C. (Ed.), Part I - Production and Standardization of Validation Reference Data. Committee on Earth Observation Satellites, USA, pp. 1–11. https://lpvs.gsfc.nasa.gov/PDF/BurnedAreaValidationProtocol.pdf.

Boschetti, L., Roy, D.P., Justice, C.O., Humber, M.L., 2015. MODIS–Landsat fusion for large area 30m burned area mapping. Remote Sens. Environ. 161, 27–42. https://doi.org/10.1016/j.rse.2015.01.022.

Boschetti, L., Stehman, S.V., Roy, D.P., 2016. A stratified random sampling design in space and time for regional to global scale burned area product validation. Remote Sens. Environ. 186, 465–478. https://doi.org/10.1016/j.rse.2016.09.016.

Brown, T.J., Hall, B.L., Mohrle, C.R., Reinbold, H.J., 2002. Coarse assessment of federal wildland fire occurrence data. In: Report for the National Wildfire Coordinating Group. Program for Climate, Ecosystem, and Fire Applications Report 02-04. Desert Research Institute, Reno, NV, USA 31 pp.

Chuvieco, E., Congalton, R.G., 1988. Mapping and inventory of forest fires from digital processing of TM data. Geocarto International 3, 41–53. https://doi.org/10.1080/10106048809354180.

Chuvieco, E., Martín, M., Palacios, A., 2002. Assessment of different spectral indices in

the red-near-infrared spectral domain for burned land discrimination. Int. J. Remote Sens. 23, 5103–5110. https://doi.org/10.1080/01431160210153129.
Chuvieco, E., Yue, C., Heil, A., Mouillot, F., Alonso-Canas, I., Padilla, M., Pereira, J., Oom, D., Tansey, K., 2016. A new global burned area product for climate assessment of fire impacts. Glob. Ecol. Biogeogr. 25, 619–629. https://doi.org/10.1111/geb.12440.
Chuvieco, E., Lizundia-Loiola, J., Pettinari, M., Ramo, R., Padilla, M., Tansey, K., Mouillot, F., Laurent, P., Storm, T., Heil, A., Plummer, S., 2018. Generation and analysis of a new global burned area product based on MODIS 250 m reflectance bands and thermal anomalies. Earth System Science Data 10, 2015–2031. https://doi.org/10.5194/essd-10-2015-2018.
Chuvieco, E., Mouillot, F., van der Werf, G.R., Miguel, J., Tanasse, M., Koutsias, N., García, M., Yebra, M., Padilla, M., Gitas, I., Heil, A., Hawbaker, T.J., Giglio, L., 2019. Historical background and current developments for mapping burned area from satellite Earth observation. Remote Sens. Environ. 225, 45–64. https://doi.org/10.1016/j.rse.2019.02.013.
Cochran, W.G., 1977. Sampling techniques, 3rd ed. John Wiley & Sons, New York, NY, USA978-0471162407 ISBN-13.
Cohen, W.B., Yang, Z., Kennedy, R.E., 2010. Detecting trends in forest disturbance and recovery using yearly Landsat time series: 2. TimeSync – tools for calibration and validation. Remote Sens. Environ. 114, 2911–2924. https://doi.org/10.1016/j.rse.2010.07.010.
Cohen, W.B., Yang, Z., Healey, S.P., Kennedy, R.E., Gorelick, N., 2018. A LandTrendr multispectral ensemble for forest disturbance detection. Remote Sens. Environ. 205, 131–140. https://doi.org/10.1016/j.rse.2017.11.015.
Dennison, P.E., Brewer, S.C., Arnold, J.D., Moritz, M.A., 2014. Large wildfire trends in the western United States, 1984–2011. Geophys. Res. Lett. 41, 2928–2933. https://doi.org/10.1002/2014gl059576.
Dwyer, J.L., Roy, D.P., Sauer, B., Jenkerson, C.B., Zhang, H.K., Lymburner, L., 2018. Analysis ready data: enabling analysis of the Landsat archive. Remote Sens-basel 10, 1363. https://doi.org/10.3390/rs10091363.
Egorov, A.V., Roy, D.P., Zhang, H.K., Li, Z., Yan, L., Huang, H., 2019. Landsat 4, 5 and 7 (1982 to 2017) Analysis Ready Data (ARD) observation coverage over the Conterminous United States and implications for terrestrial monitoring. Remote Sens. 11, 447. https://doi.org/10.3390/rs11040447.
Eidenshink, J., Schwind, B., Brewer, K., Zhu, Z.-L., Quayle, B., Howard, S., 2007. A project for monitoring trends in burn severity. Fire Ecology 3, 3–21. https://doi.org/10.4996/fireecology.0301003.
Elith, J., Leathwick, J., Hastie, T., 2008. A working guide to boosted regression trees. J. Anim. Ecol. 77, 802–813. https://doi.org/10.1111/j.1365-2656.2008.01390.x.
Epting, J., Verbyla, D., Sorbel, B., 2005. Evaluation of remotely sensed indices for assessing burn severity in interior Alaska using Landsat TM and ETM+. Remote Sens. Environ. 96, 328–339. https://doi.org/10.1016/j.rse.2005.03.002.
Frantz, D., 2019. FORCE—Landsat + Sentinel-2 analysis ready data and beyond. Remote Sens. 11, 1124. https://doi.org/10.3390/rs11091124.
Fraser, R.H., Li, Z., Cihlar, J., 2000. Hotspot and NDVI differencing synergy (HANDS): A new technique for burned area mapping over boreal forest. Remote Sensing of Environment 74, 362–376.
French, N.H., McKenzie, D., Erickson, T., Koziol, B., Billmire, M., Endsley, A.K., Scheinerman, N.K., Jenkins, L., Miller, M., Ottmar, R., Prichard, S., 2014. Modeling regional-scale wildland fire emissions with the Wildland Fire Emissions Information System. Earth Interact. 18, 1–26. https://doi.org/10.1175/EI-D-14-0002.1.
Fusco, E.J., Finn, J.T., Abatzoglou, J.T., Balch, J.K., Dadashi, S., Bradley, B.A., 2019. Detection rates and biases of fire observations from MODIS and agency reports in the conterminous United States. Remote Sens. Environ. 220, 30–40. https://doi.org/10.1016/j.rse.2018.10.028.
Gao, B., 1996. NDWI—a normalized difference water index for remote sensing of vegetation liquid water from space. Remote Sens. Environ. 58, 257–266. https://doi.org/10.1016/s0034-4257(96)00067-3.
García, M.J., Caselles, V., 1991. Mapping burns and natural reforestation using thematic Mapper data. Geocarto International 6, 31–37. https://doi.org/10.1080/10106049109354290.
Ghimire, B., Williams, C.A., Collatz, J.G., Vanderhoof, M., 2012. Fire-induced carbon emissions and regrowth uptake in western U.S. forests: documenting variation across forest types, fire severity, and climate regions. J. Geophys. Res. Biogeosci. 2005 (117). https://doi.org/10.1029/2011jg001935. n/a-n/a.
Giglio, L., Loboda, T., Roy, D.P., Quayle, B., Justice, C.O., 2009. An active-fire based burned area mapping algorithm for the MODIS sensor. Remote Sens. Environ. 113, 408–420. https://doi.org/10.1016/j.rse.2008.10.006.
Giglio, L., Randerson, J., van der Werf, G., Kasibhatla, P., Collatz, G., Morton, D., DeFries, R., 2010. Assessing variability and long-term trends in burned area by merging multiple satellite fire products. Biogeosciences 7, 1171–1186. https://doi.org/10.5194/bg-7-1171-2010.
Giglio, L., Schroeder, W., Justice, C.O., 2016. The collection 6 MODIS active fire detection algorithm and fire products. Remote Sens. Environ. 178, 31–41. https://doi.org/10.1016/j.rse.2016.02.054.
Giglio, L., Boschetti, L., Roy, D.P., Humber, M.L., Justice, C.O., 2018. The collection 6 MODIS burned area mapping algorithm and product. Remote Sens. Environ. 217, 72–85. https://doi.org/10.1016/j.rse.2018.08.005.
Goodwin, N.R., Collett, L.J., 2014. Development of an automated method for mapping fire history captured in Landsat TM and ETM+ time series across Queensland, Australia. Remote Sens. Environ. 148, 206–221. https://doi.org/10.1016/j.rse.2014.03.021.
Gorelick, N., Hancher, M., Dixon, M., Ilyushchenko, S., Thau, D., Moore, R., 2017. Google Earth Engine: planetary-scale geospatial analysis for everyone. Remote Sens. Environ. 202, 18–27. https://doi.org/10.1016/j.rse.2017.06.031.
Grady, L., 2001. Random walks for image segmentation. IEEE Trans. Pattern Anal. Mach. Intell. 28, 1768–1783. https://doi.org/10.1109/tpami.2006.233.
Hansen, M.C., Egorov, A., Potapov, P.V., Stehman, S.V., Tyukavina, A., Turubanova, S.A., Roy, D.P., Goetz, S.J., Loveland, T.R., Ju, J., Kommareddy, A., Kovalskyy, V., Forsyth, C., Bents, T., 2014. Monitoring conterminous United States (CONUS) land cover change with Web-Enabled Landsat Data (WELD). Remote Sens. Environ. 140, 466–484. https://doi.org/10.1016/j.rse.2013.08.014.
Harris, S., Veraverbeke, S., Hook, S., 2011. Evaluating spectral indices for assessing fire severity in chaparral ecosystems (Southern California) using MODIS/ASTER (MASTER) airborne simulator data. Remote Sens. 3, 2403–2419. https://doi.org/10.3390/rs3112403.
Hastie, T., Tibshirani, R., Friedman, J., 2009. The Elements of Statistical Learning Data Mining, Inference, and Prediction, ISBN-13: 978-0387848570. Springer, New York, NY, USA.
Hawbaker, T.J., Radeloff, V.C., Syphard, A.D., Zhu, Z., Stewart, S.I., 2008. Detection rates of the MODIS active fire product in the United States. Remote Sens. Environ. 112, 2656–2664. https://doi.org/10.1016/j.rse.2007.12.008.
Hawbaker, T.J., Vanderhoof, M.K., Beal, Y.-J., Takacs, J.D., Schmidt, G.L., Falgout, J.T., Williams, B., Fairaux, N.M., Caldwell, M.K., Picotte, J.J., Howard, S.M., Stitt, S., Dwyer, J.L., 2017. Mapping burned areas using dense time-series of Landsat data. Remote Sens. Environ. 198, 504–522. https://doi.org/10.1016/j.rse.2017.06.027.
Hawbaker, T.J., Vanderhoof, M.K., Schmidt, G.L., Beal, Y.-J., Picotte, J.J., Takacs, J.D., Falgout, J.T., Dwyer, J.L., 2020. The Landsat Burned Area products for the conterminous United States. U.S. Geological Survey Data Release, Science Base Catalog. https://doi.org/10.5066/P9QKHKTQ.
Holden, Z., Smith, A., Morgan, P., Rollins, M., Gessler, P., 2005. Evaluation of novel thermally enhanced spectral indices for mapping fire perimeters and comparisons with fire atlas data. International Journal of Remote Sens 26, 4801–4808. https://doi.org/10.1080/01431160500239008.
Hollmann, R., Merchant, C., Saunders, R., Downy, C., Buchwitz, M., Cazenave, A., Chuvieco, E., Defourny, P., de Leeuw, G., Forsberg, R., Holzer-Popp, T., Paul, F., Sandven, S., Sathyendranath, S., van Roozendael, M., Wagner, W., 2013. The ESA climate change initiative: satellite data records for essential climate variables. Bull. Am. Meteorol. Soc. 94, 130313072241002. https://doi.org/10.1175/bams-d-11-00254.1.
Huang, C., Goward, S.N., Masek, J.G., Thomas, N., Zhu, Z., Vogelmann, J.E., 2010. An automated approach for reconstructing recent forest disturbance history using dense Landsat time series stacks. Remote Sens. Environ. 114, 183–198. https://doi.org/10.1016/j.rse.2009.08.017.
Huang, H., Roy, D.P., Boschetti, L., Zhang, H.K., Yan, L., Kumar, S., Gomez-Dans, J., Li, J., 2016. Separability analysis of Sentinel-2A multi-spectral instrument (MSI) data for burned area discrimination. Remote Sens. 8, 873. https://doi.org/10.3390/rs8100873.
Huete, A., 1988. A soil-adjusted vegetation index (SAVI). Remote Sens. Environ. 25, 295–309. https://doi.org/10.1016/0034-4257(88)90106-x.
Huete, A., Didan, K., Miura, T., Rodriguez, E., Gao, X., Ferreira, L., 2002. Overview of the radiometric and biophysical performance of the MODIS vegetation indices. Remote Sens. Environ. 83, 195–213. https://doi.org/10.1016/s0034-4257(02)00096-2.
Jones, J.W., 2015. Efficient wetland surface water detection and monitoring via Landsat: comparison with in situ data from the Everglades depth estimation network. Remote Sens. 7, 12503–12538. https://doi.org/10.3390/rs70912503.
Jones, J., 2019. Improved automated detection of subpixel-scale inundation—revised Dynamic Surface Water Extent (DSWE) partial surface water tests. Remote Sens. 11, 374. https://doi.org/10.3390/rs11040374.
Kennedy, R.E., Yang, Z., Cohen, W.B., 2010. Detecting trends in forest disturbance and recovery using yearly Landsat time series: 1. LandTrendr — temporal segmentation algorithms. Remote Sens. Environ. 114, 2897–2910. https://doi.org/10.1016/j.rse.2010.07.008.
Key, C.H., Benson, N.C., 2006. Landscape assessment: remote sensing of severity, the Normalized Burn Ratio. In: Lutes, D.C. (Ed.), FIREMON: Fire Effects Monitoring and Inventory System. USDA Forest Service, Rocky Mountain Research Station, Ogden, UT, USA General Technical Report, RMRS-GTR-164-CD:LA1-LA51.
Kolden, C.A., Weisberg, P.J., 2007. Assessing accuracy of manually-mapped wildfire perimeters in topographically dissected areas. Fire Ecology 3, 22–31. https://doi.org/10.4996/fireecology.0301022.
Koutsias, N., 2003. An autologistic regression model for increasing the accuracy of burned surface mapping using Landsat Thematic Mapper data. Int. J. Remote Sens. 24, 2199–2204. https://doi.org/10.1080/0143116031000082073.
Koutsias, N., Karteris, M., 1998. Logistic regression modelling of multitemporal Thematic Mapper data for burned area mapping. Int. J. Remote Sens. 19, 3499–3514. https://doi.org/10.1080/014311698213777.
Koutsias, N., Karteris, M., 2000. Burned area mapping using logistic regression modeling of a single post-fire Landsat-5 Thematic Mapper image. Int. J. Remote Sens. 21, 673–687. https://doi.org/10.1080/014311600210506.
Kovalskyy, V., Roy, D.P., 2013. The global availability of Landsat 5 TM and Landsat 7 ETM+ land surface observations and implications for global 30m Landsat data product generation. Remote Sens. Environ. 130, 280–293. https://doi.org/10.1016/j.rse.2012.12.003.
Kushla, J., Ripple, W., 1998. Assessing wildfire effects with Landsat thematic mapper data. Int. J. Remote Sens. 19, 2493–2507. https://doi.org/10.1080/014311698214587.
Lewis, A., Lymburner, L., Purss, M.B., Brooke, B., Evans, B., Ip, A., Dekker, A.G., Irons, J.R., Minchin, S., Mueller, N., Oliver, S., Roberts, D., Ryan, B., Thankappan, M., Woodcock, R., Wyborn, L., 2015. Rapid, high-resolution detection of environmental change over continental scales from satellite data – the Earth Observation Data Cube. International Journal of Digit Earth 9, 106–111. https://doi.org/10.1080/17538947.2015.1111952.

Liu, Z., Wimberly, M.C., 2015. Climatic and landscape influences on fire regimes from 1984 to 2010 in the western United States. PLoS One 10, e0140839. https://doi.org/10.1371/journal.pone.0140839.
Long, T., Zhang, Z., He, G., Jiao, W., Tang, C., Wu, B., Zhang, X., Wang, G., Yin, R., 2019. 30 m resolution global annual burned area mapping based on Landsat images and Google Earth Engine. Remote Sens. 11, 489. https://doi.org/10.3390/rs11050489.
Ludwig, G., Chu, T., Zhu, J., Wang, H., Koehler, K., 2017. Static and roving sensor data fusion for spatio-temporal hazard mapping with application to occupational exposure assessment. Annals of Applied Statistics 11, 139–160. https://doi.org/10.1214/16-aoas995.
Malakar, N.K., Hulley, G.C., Hook, S.J., Laraby, K., Cook, M., Schott, J.R., 2018. An operational land surface temperature product for Landsat thermal data: methodology and validation. Ieee T Geosci Remote 56, 5717–5735. https://doi.org/10.1109/tgrs.2018.2824828.
Masek, J.G., Vermote, E.F., Saleous, N.E., Wolfe, R., Hall, F.G., Huemmrich, K.F., Gao, F., Kutler, J., Lim, T.-K., 2006. A Landsat surface reflectance dataset for North America, 1990–2000. IEEE Geosci. Remote Sens. Lett. 3, 68–72. https://doi.org/10.1109/lgrs.2005.857030.
McFeeters, S.K., 1996. The use of the Normalized Difference Water Index (NDWI) in the delineation of open water features. Int. J. Remote Sens. 17, 1425–1432. https://doi.org/10.1080/01431169608948714.
Meddens, A., Kolden, C.A., Lutz, J.A., 2016. Detecting unburned areas within wildfire perimeters using Landsat and ancillary data across the northwestern United States. Remote Sens. Environ. 186, 275–285. https://doi.org/10.1016/j.rse.2016.08.023.
Moran, C.J., Seielstad, C.A., Cunningham, M.R., Hoff, V., Parsons, R.A., Ll, Queen, Sauerbrey, K., Wallace, T., 2019. Deriving fire behavior metrics from UAS imagery. Fire 2, 36. https://doi.org/10.3390/fire2020036.
Morisette, J.T., Baret, F., Liang, S., 2006. Special issue on global land product validation. IEEE Transactions Geosciences and Remote Sensing 44, 1695–1697. https://doi.org/10.1109/tgrs.2006.877436.
Murphy, M.A., Evans, J.S., Storfer, A., 2010. Quantifying *Bufo boreas* connectivity in Yellowstone National Park with landscape genetics. Ecology 91, 252–261. https://doi.org/10.1890/08-0879.1.
Nowell, H., Holmes, C., Robertson, K., Teske, C., Hiers, J., 2018. A new picture of fire extent, variability, and drought interaction in prescribed fire landscapes: insights from Florida government records. Geophys. Res. Lett. 45, 7874–7884. https://doi.org/10.1029/2018gl078679.
Olson, D.M., Dinerstein, E., Wikramanayake, E.D., Burgess, N.D., Powell, G.V., Underwood, E.C., D'amico, J.A., Itoua, I., Strand, H.E., Morrison, J.C., Loucks, C.J., Allnutt, T.F., Ricketts, T.H., Kura, Y., Lamoreux, J.F., Wettengel, W.W., Hedao, P., Kassem, K.R., 2001. Terrestrial ecoregions of the world: a new map of life on Earth. Bioscience 51, 933. https://doi.org/10.1641/0006-3568(2001)051[0933:teotwa]2.0.co;2.
Omernik, J.M., Griffith, G.E., 2014. Ecoregions of the conterminous United States: evolution of a hierarchical spatial framework. Environ. Manag. 54, 1249–1266. https://doi.org/10.1007/s00267-014-0364-1.
Padilla, M., Stehman, S.V., Chuvieco, E., 2014. Validation of the 2008 MODIS-MCD45 global burned area product using stratified random sampling. Remote Sens. Environ. 144, 187–196. https://doi.org/10.1016/j.rse.2014.01.008.
Padilla, M., Stehman, S.V., Ramo, R., Corti, D., Hantson, S., Oliva, P., Alonso-Canas, I., Bradley, A.V., Tansey, K., Mota, B., Pereira, J., Chuvieco, E., 2015. Comparing the accuracies of remote sensing global burned area products using stratified random sampling and estimation. Remote Sens. Environ. 160, 114–121. https://doi.org/10.1016/j.rse.2015.01.005.
Padilla, M., Olofsson, P., Stehman, S.V., Tansey, K., Chuvieco, E., 2017. Stratification and sample allocation for reference burned area data. Remote Sens. Environ. 203, 240–255. https://doi.org/10.1016/j.rse.2017.06.041.
Parthum, B., Pindilli, E., Hogan, D., 2017. Benefits of the fire mitigation ecosystem service in The Great Dismal Swamp National Wildlife Refuge, Virginia, USA. J. Environ. Manag. 203, 375–382. https://doi.org/10.1016/j.jenvman.2017.08.018.
Pengra, B.W., Stehman, S.V., Horton, J.A., Dockter, D.J., Schroeder, T.A., Yang, Z., Cohen, W.B., Healey, S.P., Loveland, T.R., 2019. Quality control and assessment of interpreter consistency of annual land cover reference data in an operational national monitoring program. Remote Sens. Environ. 238, 111261. https://doi.org/10.1016/j.rse.2019.111261.
Picotte, J.J., Peterson, B., Meier, G., Howard, S.M., 2016. 1984–2010 trends in fire burn severity and area for the conterminous US. Int. J. Wildland Fire 25, 413–420. https://doi.org/10.1071/wf15039.
Pinty, B., Verstraete, M., 1992. GEMI: a non-linear index to monitor global vegetation from satellites. Vegetatio 101, 15–20. https://doi.org/10.1007/bf00031911.
Plummer, S., Arino, O., Simon, M., Steffen, W., 2006. Establishing an Earth observation product service for the terrestrial carbon community: the Globcarbon initiative. Mitig. Adapt. Strateg. Glob. Chang. 11, 97–111. https://doi.org/10.1007/s11027-006-1012-8.
Radeloff, V.C., Helmers, D.P., Kramer, A.H., Mockrin, M.H., Alexandre, P.M., Bar-Massada, A., Butsic, V., Hawbaker, T.J., Martinuzzi, S., Syphard, A.D., Stewart, S.I., 2018. Rapid growth of the US wildland-urban interface raises wildfire risk. Proc. Natl. Acad. Sci. 107, 940–945. https://doi.org/10.1073/pnas.1718850115.
Ramo, R., García, M., Rodríguez, D., Chuvieco, E., 2018. A data mining approach for global burned area mapping. International Journal of Applied Earth Observation 73, 39–51. https://doi.org/10.1016/j.jag.2018.05.027.
Richter, R., Schläpfer, D., 2016. Atmospheric/Topographic Correction for Satellite Imagery; ATCOR-2/3 User Guide, Version 9.0.2; ReSe Applications: Langeggweg, Switzerland. Available online. http://www.rese.ch/pdf/atcor3_manual.pdf.
Roteta, E., Bastarrika, A., Padilla, M., Storm, T., Chuvieco, E., 2019. Development of a Sentinel-2 burned area algorithm: generation of a small fire database for sub-Saharan Africa. Remote Sens. Environ. 222, 1–17. https://doi.org/10.1016/j.rse.2018.12.011.
Roy, D., Frost, P., Justice, C., Landmann, T., Roux, L.J., Gumbo, K., Makungwa, S., Dunham, K., Toit, D.R., Mhwandagara, K., Zacarias, A., Tacheba, B., Dube, O., Pereira, J., Mushove, P., Morisette, J., Vannan, S.S., Davies, D., 2005. The Southern Africa Fire Network (SAFNet) regional burned-area product-validation protocol. Int. J. Remote Sens. 26, 4265–4292. https://doi.org/10.1080/01431160500113096.
Roy, D.P., Boschetti, L., Justice, C.O., Ju, J., 2008. The collection 5 MODIS burned area product — global evaluation by comparison with the MODIS active fire product. Remote Sens. Environ. 112, 3690–3707. https://doi.org/10.1016/j.rse.2008.05.013.
Roy, D.P., Wulder, M.A., Loveland, T.R., C.E., W., Allen, R.G., Anderson, M.C., Helder, D., Irons, J.R., Johnson, D.M., Kennedy, R., Scambos, T.A., Schaaf, C.B., Schott, J.R., Sheng, Y., Vermote, E.F., Belward, A.S., Bindschadler, R., Cohen, W.B., Gao, F., Hipple, J.D., Hostert, P., Huntington, J., Justice, C.O., Kilic, A., Kovalskyy, V., Lee, Z.P., Lymburner, L., Masek, J.G., McCorkel, J., Shuai, Y., Trezza, R., Vogelmann, J., Wynne, R.H., Zhu, Z., 2014. Landsat-8: science and product vision for terrestrial global change research. Remote Sens. Environ. 145, 154–172. https://doi.org/10.1016/j.rse.2014.02.001.
Roy, D.P., Kovalskyy, V., Zhang, H.K., Vermote, E.F., Yan, L., Kumar, S.S., Egorov, A., 2016. Characterization of Landsat-7 to Landsat-8 reflective wavelength and normalized difference vegetation index continuity. Remote Sens. Environ. 185, 57–70. https://doi.org/10.1016/j.rse.2015.12.024.
Roy, D.P., Huang, H., Boschetti, L., Giglio, L., Yan, L., Zhang, H.H., Li, Z., 2019. Landsat-8 and Sentinel-2 burned area mapping - a combined sensor multi-temporal change detection approach. Remote Sens. Environ. 231, 111254. https://doi.org/10.1016/j.rse.2019.111254.
Sankey, J.B., Kreitler, J., Hawbaker, T.J., McVay, J.L., Miller, M., Mueller, E.R., Vaillant, N.M., Lowe, S.E., Sankey, T.T., 2017. Climate, wildfire, and erosion ensemble foretells more sediment in western USA watersheds. Geophys. Res. Lett. 44, 8884–8892. https://doi.org/10.1002/2017gl073979.
Schroeder, W., Oliva, P., Giglio, L., Quayle, B., Lorenz, E., Morelli, F., 2016. Active fire detection using Landsat-8/OLI data. Remote Sens. Environ. 185, 210–220. https://doi.org/10.1016/j.rse.2015.08.032.
Selkowitz, D.J., Forster, R.R., 2016. Automated mapping of persistent ice and snow cover across the western U.S. with Landsat. ISPRS J. Photogramm. Remote Sens. 117, 126–140. https://doi.org/10.1016/j.isprsjprs.2016.04.001.
Shakesby, R.A., Doerr, S.H., 2006. Wildfire as a hydrological and geomorphological agent. Earth Sci. Rev. 74, 269–307. https://doi.org/10.1016/j.earscirev.2005.10.006.
Short, K., 2013. A spatial database of wildfires in the United States, 1992–2011. Earth System Science Data Discussions 6, 297–366. https://doi.org/10.5194/essdd-6-297-2013.
Short, K.C., 2015. Sources and implications of bias and uncertainty in a century of US wildfire activity data. Int. J. Wildland Fire 24, 883–891. https://doi.org/10.1071/wf14190.
Smith, A., Drake, N., Wooster, M., Hudak, A., Holden, Z., Gibbons, C., 2007. Production of Landsat ETM+ reference imagery of burned areas within Southern African savannahs: comparison of methods and application to MODIS. Int. J. Remote Sens. 28, 2753–2775. https://doi.org/10.1080/01431160600954704.
Stehman, S.V., 1997. Estimating standard errors of accuracy assessment statistics under cluster sampling. Remote Sens. Environ. 60, 258–269. https://doi.org/10.1016/s0034-4257(96)00176-9.
Stehman, S.V., 2009. Sampling designs for accuracy assessment of land cover. Int. J. Remote Sens. 30, 5243–5272. https://doi.org/10.1080/01431160903131000.
Stehman, S.V., Arora, M.K., Kasetkasem, T., Varshney, P.K., 2007. Estimation of fuzzy error matrix accuracy measures under stratified random sampling. Photogramm. Eng. Remote. Sens. 73 (9), 165–173. https://doi.org/10.14358/pers.73.2.165.
Steven, M.D., Malthus, T.J., Baret, F., Xu, H., Chopping, M.J., 2003. Intercalibration of vegetation indices from different sensor systems. Remote Sens. Environ. 88, 412–422. https://doi.org/10.1016/j.rse.2003.08.010.
Stroppiana, D., Bordogna, G., Carrara, P., Boschetti, M., Boschetti, L., Brivio, P.A., 2012. A method for extracting burned areas from Landsat TM/ETM+ images by soft aggregation of multiple Spectral Indices and a region growing algorithm. ISPRS J. Photogramm. Remote Sens. 69, 88–102. https://doi.org/10.1016/j.isprsjprs.2012.03.001.
Tansey, K., Grégoire, J., Defourny, P., Leigh, R., Pekel, J., van Bogaert, E., Bartholomé, E., 2008. A new, global, multi-annual (2000–2007) burnt area product at 1 km resolution. Geophys. Res. Lett. 35. https://doi.org/10.1029/2007gl031567.
Tran, B., Tanase, M.A., Bennett, L.T., Aponte, C., 2018. Evaluation of spectral indices for assessing fire severity in Australian temperate forests. Remote Sens. 10, 1680. https://doi.org/10.3390/rs10111680.
Trigg, S., Flasse, S., 2000. Characterizing the spectral-temporal response of burned savannah using in situ spectroradiometry and infrared thermometry. Int. J. Remote Sens. 21, 3161–3168. https://doi.org/10.1080/01431160050145045.
Trigg, S., Flasse, S., 2001. An evaluation of different bi-spectral spaces for discriminating burned shrub-savannah. Int. J. Remote Sens. 22, 2641–2647. https://doi.org/10.1080/01431160110053185.
Tucker, C.J., 1979. Red and photographic infrared linear combinations for monitoring vegetation. Remote Sens. Environ. 8, 127–150. https://doi.org/10.1016/0034-4257(79)90013-0.
Urbanski, S.P., Reeves, M.C., Corley, R.E., Silverstein, R.P., Hao, W., 2018. Contiguous United States wildland fire emission estimates during 2003–2015. Earth System Science Data 10, 2241–2274. https://doi.org/10.5194/essd-10-2241-2018.
van Wagtendonk, J.W., Root, R.R., Key, C.H., 2004. Comparison of AVIRIS and Landsat ETM+ detection capabilities for burn severity. Remote Sens. Environ. 92, 397–408. https://doi.org/10.1016/j.rse.2003.12.015.
Vanderhoof, M.K., Brunner, N., Beal, Y.-J.G., Hawbaker, T.J., 2017a. Evaluation of the

U.S. Geological Survey Landsat burned area essential climate variable across the conterminous U.S. using commercial high-resolution imagery. Remote Sens. 9, 743. https://doi.org/10.3390/rs9070743.

Vanderhoof, M.K., Fairaux, N., Beal, Y.-J.G., Hawbaker, T.J., 2017b. Validation of the USGS Landsat Burned Area Essential Climate Variable (BAECV) across the conterminous United States. Remote Sens. Environ. 198, 393–406. https://doi.org/10.1016/j.rse.2017.06.025.

Vanderhoof, M.K., Fairaux, N.M., Beail, Y., Hawbaker, T.J., 2020. Data release for the validation of the USGS Landsat burned area product across the conterminous U.S. U.S. Geological Survey data release. In: Science Base Catalog, https://doi.org/10.5066/P9QKHKTQ.

Verbesselt, J., Hyndman, R., Newnham, G., Culvenor, D., 2010. Detecting trend and seasonal changes in satellite image time series. Remote Sens. Environ. 114, 106–115. https://doi.org/10.1016/j.rse.2009.08.014.

Verhegghen, A., Eva, H., Ceccherini, G., Achard, F., Gond, V., Gourlet-Fleury, S., Cerutti, P., 2016. The potential of Sentinel satellites for burnt area mapping and monitoring in the Congo Basin forests. Remote Sens. 8, 986. https://doi.org/10.3390/rs8120986.

Vermote, E., Justice, C., Claverie, M., Franch, B., 2016. Preliminary analysis of the performance of the Landsat 8/OLI land surface reflectance product. Remote Sens. Environ. 185, 46–56. https://doi.org/10.1016/j.rse.2016.04.008.

Vogelmann, J.E., Howard, S.M., Yang, L.Y., Larson, C.R., Wylie, B.K., Van Driel, N., 2001. Completion of the 1990s National Land Cover Data set for the Conterminous United States from Landsat Thematic Mapper data and ancillary data sources. Photogramm. Eng. Remote. Sens. 65, 650–662.

Westerling, A.L., 2011. Increasing western US forest wildfire activity sensitivity to changes in the timing of spring. Philosophical Transactions Royal Society B 371, 20150178. https://doi.org/10.1098/rstb.2015.0178.

Wilson, E., Sader, S.A., 2002. Detection of forest harvest type using multiple dates of Landsat TM imagery. Remote Sens. Environ. 80, 385–396. https://doi.org/10.1016/s0034-4257(01)00318-2.

Wulder, M.A., Loveland, T.R., Roy, D.P., Crawford, C.J., Masek, J.G., Woodcock, C.E., Allen, R.G., Anderson, M.C., Belward, A.S., Cohen, W.B., Dwyer, J., Erb, A., Gao, F., Griffiths, P., Helder, D., Hermosilla, T., Hipple, J.D., Hostert, P., Hughes, J.M., Huntington, J., Johnson, D.M., Kennedy, R., Kilic, A., Li, Z., Lymburner, L., McCorkel, J., Pahlevan, N., Scambos, T.A., Schaaf, C., Schott, J.R., Sheng, Y., Storey, J., Vermote, E., Vogelmann, J., White, J.C., Wynne, R.H., Zhu, Z., 2019. Current status of Landsat program, science, and applications. Remote Sens. Environ. 225, 127–147. https://doi.org/10.1016/j.rse.2019.02.015.

Yang, L., Jin, S., Danielson, P., Homer, C., Gass, L., Bender, S.M., Case, A., Costello, C., Dewitz, J., Fry, J., Funk, M., Granneman, B., Liknes, G.C., Rigge, M., Xian, G., 2018. A new generation of the United States National Land Cover Database: requirements, research priorities, design, and implementation strategies. ISPRS J. Photogramm. Remote Sens. 146, 108–123. https://doi.org/10.1016/j.isprsjprs.2018.09.006.

Zhu, Z., Woodcock, C.E., 2012. Object-based cloud and cloud shadow detection in Landsat imagery. Remote Sens. Environ. 118, 83–94. https://doi.org/10.1016/j.rse.2011.10.028.

Zhu, Z., Woodcock, C.E., 2014a. Continuous change detection and classification of land cover using all available Landsat data. Remote Sens. Environ. 144, 152–171. https://doi.org/10.1016/j.rse.2014.01.011.

Zhu, Z., Woodcock, C.E., 2014b. Automated cloud, cloud shadow, and snow detection in multitemporal Landsat data: an algorithm designed specifically for monitoring land cover change. Remote Sens. Environ. 152, 217–234. https://doi.org/10.1016/j.rse.2014.06.012.

Zhu, Z., Zhang, J., Yang, Z., Aljaddani, A.H., Cohen, W.B., Qiu, S., Zhou, C., 2019. Continuous monitoring of land disturbance based on Landsat time series. Remote Sens. Environ. 238 (1), 111116.